Department of Physics and Astronomy
Heidelberg University

Bachelor Thesis in Physics
submitted by

Joshua Marks

born in Minden (Germany)

2022

A Low Cost Digital Camera as Thermal Camera for Volcanic Applications

This Bachelor Thesis has been carried out by Joshua Marks at the
Institute for Environmental Physics (IUP) in Heidelberg
under the supervision of
Prof. Ulrich Platt

Abstract

The lava temperature is an important characteristic quantity of a volcano. It is closely linked with the composition of the magma and the volcanic activity. It also partly affects the composition of volcanic gases, which are of great interest because of their influence on short therm atmospheric processes and climate. Thus, measurements of the temperature of lava are important for many volcanic studies.
Most of the commercially available thermal cameras, which work in the relevant temperature range of about 600 to 1100 °C, are rather expensive. This study shows, that with alternative approaches, that are based on the sensitivity of the silicon based sensors of consumer digital cameras in the near-infrared (up to about 1100 nm), temperatures of ca. 500 °C and higher can be measured.
In this thesis a compact digital consumer camera is used for the measurement of the temperature distribution of lava with high spatial resolution (16 MP). The camera was modified to block the visible spectrum and the characteristics of the remaining color filter (Bayer filter) are used to infer temperature from differential intensities. To do so a calibration with a heating wire is performed within the temperature range of 600 to 1100 °C, which demonstrated the feasibility of temperature measurements with sufficient accuracy. Besides the low costs, superior mobility and simple handling, the high spatial resolution allows for temperature measurements even in highly dynamic situations.

Zusammenfassung

Die Temperatur von Lava ist eine wichtige charakteristische Größe von einem Vulkan. Sie hängt eng mit der Zusammensetzung der Magma und der vulkanischen Aktivität zusammen. Außerdem beeinflusst sie unter anderem die Zusammensetzung der vulkanischen Gase. Diese sind aufgrund ihres kurzfristigen Einflusses auf atmosphärische Prozesse und das Klima von großem Interesse. Messungen der Lavatemperatur sind folglich für viele Studien von Vulkanen wichtig.
Die meisten kommerziell erhältlichen thermalen Kameras, welche in dem relevanten Temperaturbereich von ca. 600 bis 1100 °C arbeiten, sind eher teuer. Zudem ist die räumliche Auflösung zumeist recht beschränkt. Diese Arbeit zeigt, dass mit alternativen Ansätzen, welche auf der Sensitivität der Silizium-basierten Sensoren von herkömmlichen Digitalkameras im nahinfraroten Bereich (bis ca. 1100 nm) basieren, Temperaturen ab ca. 500 °C gemessen werden können.
In dieser Arbeit wird eine kompakte Digitalkamera zur Messung der Temperaturverteilung von Lava mit hoher räumlicher Auflösung (16 MP) vorgestellt. Die Kamera wurde modifiziert, sodass das sichtbare Spektrum blockiert wird, und die Eigenschaften der verbliebenen Farbfilter (Bayer-Filter) werden genutzt, um mit differentiellen Intensitäten auf die Temperatur zu schließen. Dazu wird eine Kalibration mit einem Heizdraht im Temperaturbereich von 600 bis 1100 °C durchgeführt, was die Realisierbarkeit von Temperaturmessungen mit hinreichender Genauigkeit demonstriert. Neben den geringen Kosten, der hervorragenden Mobilität und der einfachen Handhabung, erlaubt die hohe Auflösung Temperaturmessungen auch in hochdynamischen Situationen.

Contents

1 Introduction

Temperature of lava is an important quantity in volcanic applications. It is for instance a crucial parameter for reaching a better understanding of the evolution of volcanic gas emissions driven by chemical reactions inside volcanic plumes, that are dependent on the emission temperature. There are many reports on the influence of volcanic gases on the climate and atmospheric processes. To investigate high-temperature (>500 °C) gas chemistry the species distributions were modelled by a number of authors, for instance by Gerlach [2004] (especially for ozone depleting trace gases), Roberts et al. [2019] and others. Gas emissions are also influenced by the eruptive style as it is described by Oppenheimer et al. [2018]. The eruptive style also influences the lava temperature at the surface.

The radiative temperature is often measured and the radiative power output of volcanoes is calculated [see e.g. Wilkes et al., 2018]. Near-infrared (NIR) and infrared (IR) sensors are often used to do so [see e.g. Flynn et al., 1993]. Remote measurements are preferable, because of the high temperatures of the lava and also the toxicity of the volcanic gas emissions. The instruments commonly used for these measurements are often quite expensive and have a limited spatial resolution, and operate in mid- to long-wavelength-IR.

An alternative to these systems are commercially available cameras with silicon sensors. Their sensors are sensitive in the NIR and hence can be used for high-temperature thermal imaging applications. An example for such an application is given by Wilkes et al. [2018]. There a "Raspberry Pi" camera module was modified to serve as a NIR thermal camera. The Bayer filter, which is used to provide color information in all consumer camera sensors, was removed and a dedicated optical system was built. The data of the camera sensor is recorded to be used for the temperature determination. For the calibration a black body furnace was used.

In order to obtain an insight of the disadvantages and advantages of the method used by Wilkes et al. [2018] and similar methods a brief overview is given in the following [see also Wilkes et al., 2018]. Because of Planck's law, less light is emitted at shorter wavelengths for lower temperatures. Hence the NIR cameras are only practicable for higher temperatures (several hundred degrees Celsius) in contrast to mid- and long-IR systems. NIR sunlight reflected from the observed object will have a larger impact on the measurement and aerosols could lead to more scattering of the light, compared to systems operating in long-wavelength-IR. However, a big advantage of using commercially available cameras, besides the low price, is the high spatial resolution. Additionally, the control by the user is quite good. The saturation of the sensors can be easily regulated by the shutter speed and the size of the aperture (which is characterized by the F-number), so there is a large dynamic range. And in general, the 'point and shoot' principle and the mobility of these cameras is advantageous for usage.

In this thesis a commercially available camera is used as a high-temperature thermal camera. In contrast to Wilkes et al. [2018] a decisive modification was made. As it is also quite often done for artistic purposes the 'hot mirror', which is an optical filter that is only transparent for visible

light and reflects IR, was replaced by an IR pass filter. In combination with the Bayer filter, which was not removed in this thesis, this leads to some different effects for images taken with this setup [see e.g. Mangold et al., 2013]. The ratio of the red and the blue channel of the Bayer filter was investigated. Because of Planck's law and the different transmission of the color filters of the Bayer filter in the NIR the ratio of the red and the blue channels can be used to calculate the radiative temperature of an object. Using the ratio of the red and the blue channel and its dependency on the temperature is more stable compared to the mostly used method of measuring an absolute intensity value, because most of the effects, that affect the absolute value, are likely to appear for both channels equally. Because the exact filter curves of these color filters are unknown, a calibration is needed. This calibration was performed by observing a heating wire, where the temperature of the wire was calculated from the applied current. To use this method it is necessary to have a camera, where the images are accessible in a raw image format. Otherwise the images undergo on-chip postprocessing. Different manufacturers use different raw image types. The digital camera COOLPIX A from Nikon used in this thesis supports the format .NEF [Nikon, 2013], which can be read out with the *rawpy* [Riechert, 2014] package in Python3.

2 Theoretical Background

2.1 Thermal Radiation

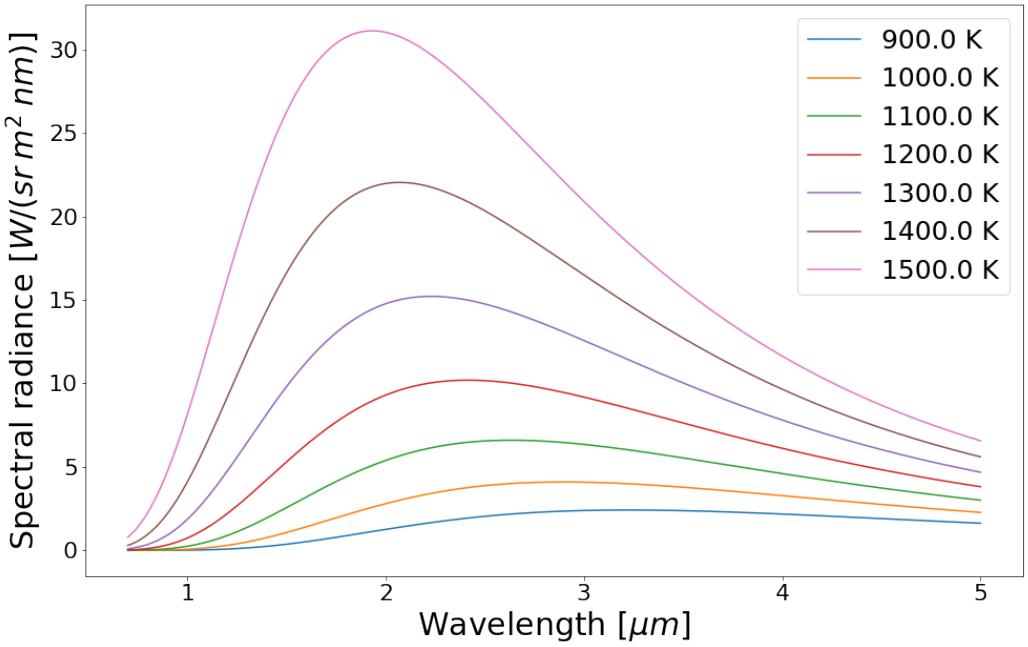

Figure 1: Planck curves of the spectral radiance B for different temperatures related to Eq. (1).

Every object emits thermal radiation in form of electromagnetic waves. For a black body at a temperature T the emitted radiation is given by Planck's law. A black body is characterized by the fact, that it absorbs all incident light [Demtröder, 2015]. The spectral radiance B per unit area and per unit solid angle for a certain wavelength λ then reads

$$B(\lambda, T) = \frac{2hc^2}{\lambda^5} \frac{1}{e^{\frac{hc}{\lambda k_B T}} - 1}. \tag{1}$$

Here h is the Planck constant, c is the speed of light and k_B is the Boltzmann constant. The maximum of this emitted spectrum shifts towards larger wavelengths for lower temperatures and the total emitted energy decreases. As example some Planck curves are shown in Fig. 1 for different temperatures. [for more detailed information see e.g. Demtröder, 2016]
For temperatures of 600 to 1100 °C, investigated in this thesis, the maximum of the Planck spectra is at longer wavelengths than the wavelengths accessible by the sensors. Hence only a small part of the distribution from Planck's law is investigated, but because of the change of the distributions with the temperature there are still measurable differences for different temperatures.
The total power that is emitted by a black body is proportional to T^4 according to the Stefan-Boltzmann law. If the emitting body is not a black body there will be less emission of energy than for a black body. This is characterised by the emissivity ε ranging between 0 and 1. For an object, which is no black body, the total emitted power reads

$$P = \varepsilon \sigma A T^4. \tag{2}$$

Where σ is the Stefan-Boltzmann constant, A is the surface area of the emitting object and T is the temperature of the object. [Demtröder, 2015], [Stefan, 1879]
Another kind of energy transport is the transport through a body. Thermal conduction is generated by colliding particles, which transfer their energy through collisions. The heat flow $\dot{Q}$ can be calculated as follows

$$\dot{Q}_A = \frac{\kappa A}{l} (T - T_0). \tag{3}$$

Where κ is the thermal conductivity of the material, in which the conduction takes place, l is the length of the object with two ends with temperatures of T and T_0. [Demtröder, 2015]

2.2 Camera Sensors

A camera sensor is a solid state electronic device consisting of a photo detector and transistors. There are many different kinds of such sensors. In general the incident light creates a signal, because of the photosensitive characteristics of the used materials, which is further amplified and ultimately converted into a digital number. This number only represents the light intensity and does not include color information [Maschal et al., 2010]. Because of the differential approach

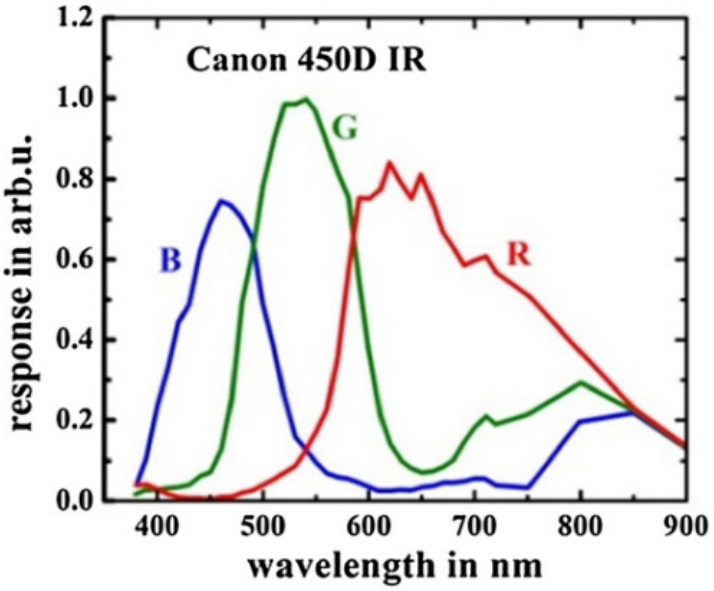

Figure 2: As an example the response of a detector of a Canon EOS 450 DSLR. The IR-blocking filter is removed, so that the response reflects the filter curves. The figure is taken from Mangold et al. [2013], Figure 2 (c).

in this thesis, only the digital numbers and the used filters are from interest. [For an insight into the large topic, camera sensors, see for instance the review from Fossum and Hondongwa, 2014]

To capture an image the color information is crucial. This information is not collected by the camera sensors itself. To collect the color information combinations of filters are used. In general there is a filter, which only transmits light in the visible range while longer wavelengths are reflected, the so called 'hot mirror'. This is done to detect a similar wavelength range as the human eye does, so that the images reflect the human perception. This filter can be exchanged as it is often done for artistic reasons, because a different filter leads to different colors of the same objects. The color information is often received by the usage of a second filter, most commonly by the usage of a Bayer filter. The Bayer filter consists of a pattern of different color filters, the so called Bayer pattern, that directly covers the single image sensors, the pixels. The most common colors are red, green and blue. [Bayer, July 1976]

The single color filters only transmit for light in the wavelength range associated with the color. An example for the filter curves can be seen in Fig. 2. So every pixel has the color information of its corresponding filter. The filter also transmit in the near-infrared, for which reason the previously mentioned filter is important. The most common Bayer pattern is shown in Fig. 3. Here the smallest repeating part of a 2x2 pixel area is covered by one blue (top left), one red (bottom right) an two green (top right and bottom left) filters. This pattern then repeats itself over the rest of the sensors. The green filter is present twice, because the human perception is more sensitive for this color. [Bayer, July 1976], [Maschal et al., 2010]

The color information stored in the single pixels can then be used to recreate a color image. For

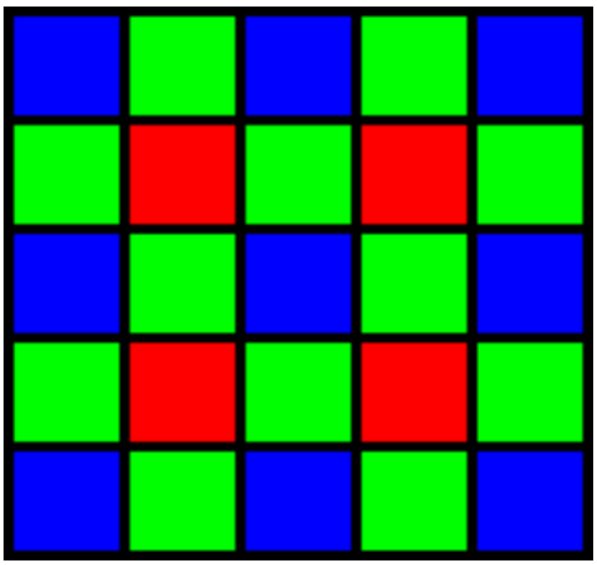

Figure 3: Typical Bayer pattern with red, green and blue color filters. The figure is taken from Maschal et al. [2010].

this purpose many different algorithms with different strengths and weaknesses exist [see e.g. Maschal et al., 2010]. This so called postprocessing combines all of the single pixel values in various ways to create a final color image as it is known from digital cameras. In this thesis the raw image, the image before postprocessing and the direct color information, is from further interest.

2.3 Flat Field Correction and Integrating Spheres

A flat field correction (FFC) is used to correct for inhomogeneities in the detector pixel response. For a digital camera, as it is used in this thesis, effects like the vignetting, dust and scratches on the sensor and the variation of the pixel sensitivities will be corrected [Wilkes et al., 2018]. For this FFC a flat field image for every F-number (which represents the size of the aperture) has to be acquired. A flat field image is an image, which is equally illuminated, so that the only differences in the captured images are due to the inhomogeneities of the sensor. Also a dark field is needed, which is an image without any incident light. Using the formula

$$C = \frac{(R-D)\cdot m}{F-D} = (R-D)\cdot G, \; with \; m = \overline{F-D}, \tag{4}$$

where C is the corrected image, R is the raw image (the uncorrected image), F the flat field image, D the dark field, $G = \frac{m}{(F-D)}$ is the so called gain and m is the averaged value of all single pixel values of a flat field image minus a dark field, the images can be corrected. [As an example for a FFC in X-ray imaging see e.g. Nieuwenhove et al., 2015]
For a FFC with digital cameras an integrating sphere is mostly used for recording the flat field image. An integrating sphere is a sphere with an inner surface that is diffuse-reflecting with

a reflectivity close to unity. Light from the light sources that enters the sphere through the apertures is reflected many times before it exits again. So at the output port, where the image with the camera is taken, the emanating light intensity is spatially uniform. For an example of this principle see e.g. Ducharme et al. [1997], where an integrating sphere is designed and built.

3 Measurement Principle

The measurement principle is based on the filter characteristics in the NIR. As it can be seen in Fig. 2 the filter curves of the red and the blue filters are different in the range of visible light, but also in the NIR. Detailed filter curves for the used camera could not be found and so the exact filter curves are unknown (the filter curves in Fig. 2 are only an example). In general the red filter still transmits at the cut off wavelength of the 'hot mirror' and towards longer wavelengths with decreasing transmissivity, while the blue filter does not or almost not transmit at the cut off wavelength and again transmits for longer wavelengths mostly with similar transmissivity as the red filter (see Fig. 2). [see e.g. Mangold et al., 2013]
The rb-ratio is the red intensity value from the red pixels divided by the blue intensity value from the corresponding blue pixel. As it is known from Planck's law (Eq. (1)) there are different amounts of incident light on the sensors for different wavelengths emitted by a black body radiator. Because of the different transmissions of the red and blue filters the rb-ratio is not equal to unity (compare Fig. 2 and also Fig. 4). At different temperatures the amount of incident light per wavelength also changes (see Fig. 1) and thus the rb-ratio as well. The resulting dependency enables to determine the temperature by calculating the rb-ratio.

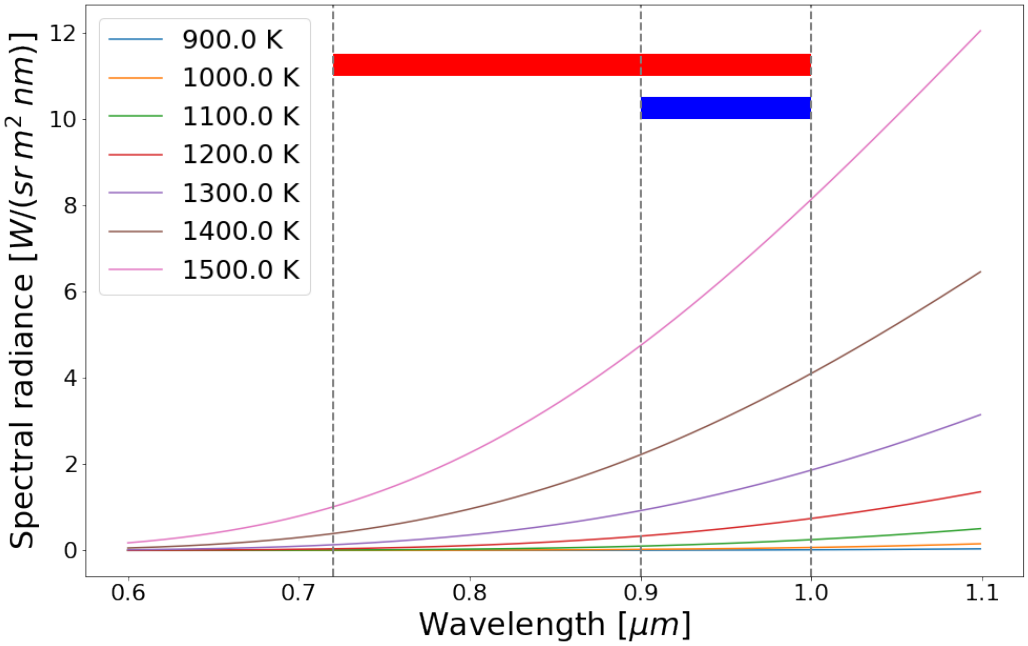

Figure 4: The different filter ranges of the red and blue filter in the NIR with simplified assumptions for the filters. The red filter transmits within 720 to 1000 nm (red line) and the blue filter within 900 to 1000 nm (blue line). The transmissivities of the filters are assumed to be 100 % in their respective ranges, that are shown over Planck curves for different temperatures.

To visualize this dependency a simplified model was developed. In this model the simplified

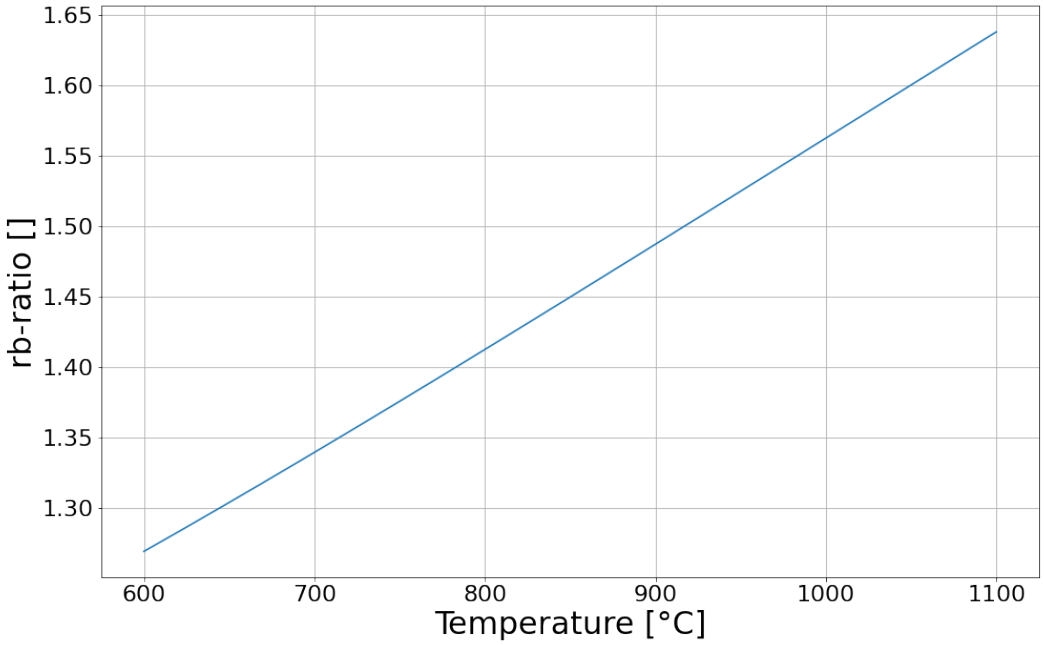

Figure 5: The rb-ratio as a function of the temperature due to the different assumed filter characteristics of the simplified model, as it is explained in the text.

filter transmission coefficients were assumed. The lower cut off wavelength for shorter wavelengths due to the NIR-filter was assumed to be 720 nm, the upper cut off wavelength is assumed to be 1000 nm. It was assumed that the red filter transmits within this range and the blue filter only transmits (in the NIR) within 900 to 1000 nm. The transmissivity is assumed to be 100 % in the respective ranges of the filter and zero at any other wavelength. A visualisation of the assumed transmissivities with Planck curves can be seen in Fig. 4. The resulting dependency of the rb-ratio on the temperature is shown in Fig. 5. The form of this dependency also could be different because of different filter curves regarding the range and the efficiency of the transmissivity.

In general the spatial distance of the red and blue pixel that belong together and therefore the spots of the photographed object should be as small as possible to get the best spatial distribution of the rb-ratios. For the pattern rggb the corresponding blue value is one row and one column further in the raw image, so that this pixel belongs to the same cut out of the Bayer pattern as the red pixel. Hence the resolution is the rb-ratios is half as large as that of the raw image without the additional columns and rows itself.

In Fig. 6 the dependency of the rb-ratio on the red value, still related to the simplified model, is shown. The red value is plotted on a logarithmic scale and was calculated as the integral of Planck's law over the wavelength range (720 - 1000 nm), where the red filter transmits. They differ in the absolute value from the red values, that will be measured, but do not change the dependency itself. This dependency is interesting, because in general the amount of incident light

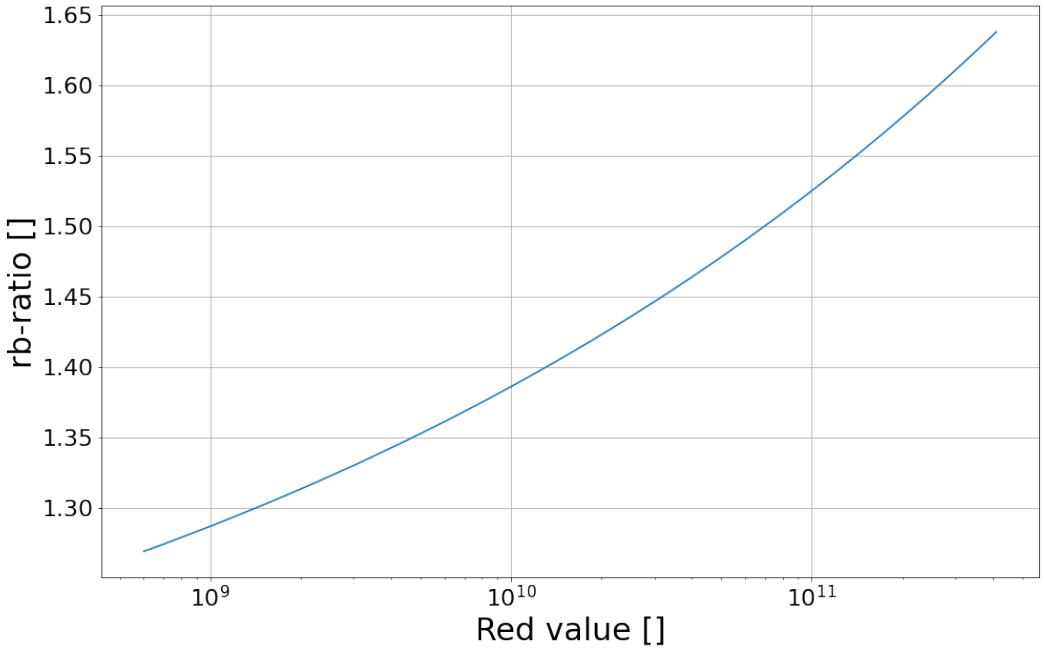

Figure 6: The rb-ratio as a function of the red value due to the different assumed filter characteristics of the simplified model, as it is explained in the text. With a logarithmic scale for the red value.

and therefore the red value is higher for higher temperatures. Hence the rb-ratio also should change with the red value, as it does in the simplified model.

This model shows that in principle a determination of the temperature of an object with the calculation of the rb-ratio from a taken image of this object is possible. Because of the unknown form of the filter curves an exact calculation of the dependency with this model is not practicable. Hence a calibration for the used camera was done. This calibration will be described in section 5.

4 Camera Setup

A COOLPIX A digital camera from Nikon is used in this thesis. A picture of the camera can be seen in Fig. 7. [Nikon, 2013]

Figure 7: Picture of the COOLPIX A digital camera from Nikon. The dimensions of the camera are approximately 11 cm x 6.5 cm x 4 cm.

The filter, which is located behind the optics of the camera and in front of the camera sensor with the Bayer pattern and which influences all pixels similarly, was replaced. The original filter only transmits the wavelengths in the visible range and cuts of the near infrared (NIR) radiation and longer wavelengths (ca. >700 nm), while the used filter works the other way around. The new filter cuts off wavelengths shorter than 720 nm. [compare e.g. Mangold et al., 2013]
The pictures taken with this camera have the format .JPG with a resolution of 4928x3264 pixels in the high quality setting (without binning). Also the camera allows the access of the raw images of the taken pictures. They are the ones of interest for this thesis, because they still include the intensity information of each individual pixel without any further post processing. The format of the raw images is .NEF and the size of .NEF files is 4992x3280.
In the additional columns and rows of the raw image further information of the camera sensor and the color pattern is saved. This information is needed for further postprocessing to create common images, as it is automatically done in digital cameras and also can be applied manually to raw images. Postprocessing changes the raw data and the color information of the individual pixels also gets lost in this process, but in this thesis the raw data and the color information is crucial. Not all but, some of the sensor information stored in the .NEF files is needed for

the data analysis described in section 5.2. The most important information is the color pattern, which is rggb (same pattern as in Fig.3, but starting with a red filter in the top left corner). Also the maximum value of the pixels is known, because the intensity of the light that reaches the sensors after passing through the different filters is recorded as a number in the range of 0 to 16383. If this maximum value is exceeded the signal is saturated.
How to work with the .NEF format and how to receive the needed information mentioned above in Python3 is explained in the Appendix.

5 Camera Calibration

5.1 Experimental Setup

In order to calibrate the camera to assign a temperature to an observed rb-ratio an experiment is needed where the temperature of an thermal radiator is known. The calculations with the simplified model (see section 3) is inaccurate. Therefore measurements with an independent determination of the temperature of the object is needed. It is of course necessary to determine several pairs of temperature and rb-ratios to get a reliable calibration. Hence a set up is needed where high temperatures of a suitable object can be set to known values.
Using a heating wire presents a cost effective way to do such a calibration for high temperatures (600 to 1100 °C). Heating wires are commonly used, they are good thermal radiators and the temperature can be adjusted in the range of interest by varying the electrical current, that is lead through it. This was done by varying the resistance of the heating wire by changing the length of it.

5.1.1 Wire Characteristics

Overall heating wires are cost effective and easy accessible because of their widespread use in home appliances and industrial furnaces. The temperatures of interest in this study are about 600 to 1100 °C. Hence, the melting point of the wire material needs to be higher than that. There are different types of alloys for several heating wires available. The most useful alloys for this application are a nickel-chromium alloy (NiCr alloy) and a iron-chromium-aluminium alloy (FeCrAl alloy). Both alloys are able to reach high temperatures without high oxidation or melting. The NiCr alloy is temperature resistant up to 1150 °C and the FeCrAl alloy is temperature resistance up to 1300 °C. The electrical resistance of this alloys is quite high and its resistance is also quite constant over a wide temperature range. Fig. 8 shows the electrical resistance of the wire KANTHAL D, which is a FeCrAl alloy and the one used in this calibration experiment.

5.1.2 Temperature Determination

In order to get an accurate calibration the knowledge of the actual temperature of the heating wire during the measurement is necessary. Quantifying such high temperatures of a thin wire is not straightforward. In the first instance, a simplified model of a thermal radiator in combination with some crucial information of the relationship between the current through the wire and the temperature was applied to achieve an sufficient accuracy.
The data sheet of the wire NI80 from OMEGA which is an NiCr alloy provides the dependency of the current on the temperature for a number of given values. They can be seen in Tab. 1 for a diameter of the wire of 1 mm. This alloy is not the one that is used for this calibration but this dependency is used to calculate the corresponding dependency of the current and the

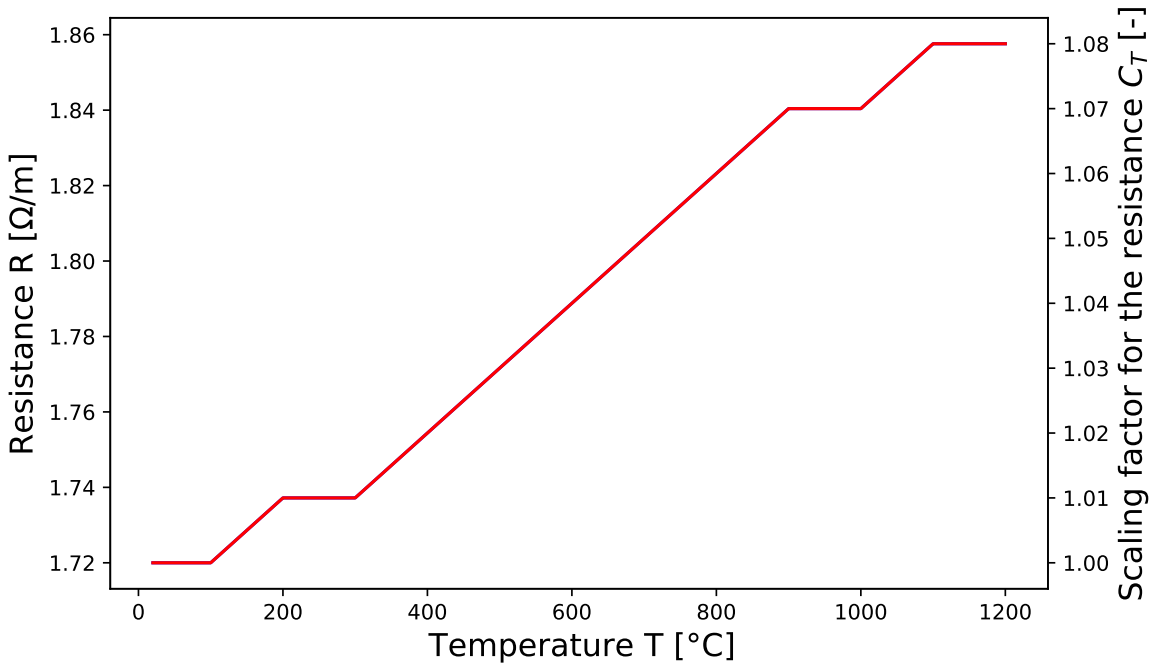

Figure 8: Resistance respectively the scaling factor for the resistance of the wire KANTHAL D. The data for this graph is taken from the data sheet for the wire KANTHAL [2016].

temperature for the used KANTHAL D alloy, because for the latter such a dependency was not accessible. The wire used in this thesis has the same diameter of 1 mm. To determine the temperature of the wire from the current, first a simplified model of thermal radiation and thermal transport for a hot wire is established.

For a given current, the wire will heat up and at the same time it will emit the energy by thermal radiation and thermal conduction. After a short up-heating phase the temperature will reach an equilibrium. In this case the supplied energy and therefore the electrical power and the thermal losses are equal:

$$P = U \cdot I = R_0 \cdot L \cdot C_T \cdot I^2 = \dot{Q}_S + \dot{Q}_L. \tag{5}$$

The supplied power P can be expressed via the current I and the voltage U. The latter can then be expressed by the resistance per meter at 20 °C R_0, the length L of the wire, the temperature factor C_T, and the current.

In general there are three types of thermal losses. These losses are the thermal radiation, the thermal conduction through air and the thermal conduction through the direct contact of the wire with its suspension. Because of the latter the temperature of the wire shows a gradient towards its ends. In the framework of this experiment the area of interest, which is the area where the measurements with the camera are done, is far enough away from these ends. So the third thermal loss term can be excluded and only the first two mentioned thermal losses are the ones of interest.

The rate of energy transfer $\dot{Q}_R$ for thermal radiation is then given by

$$\dot{Q}_R = \varepsilon\sigma A\left(T^4 - T_0^4\right) = \varepsilon\sigma\pi dL\left(T^4 - T_0^4\right), \tag{6}$$

whereas the surface area of the wire is very small and completely surrounded by the area of the ambient room. The emissivity of the alloy is ε, σ is the Stefan-Boltzmann constant, the temperatures of the alloy and the ambient air are T and T_0 while A is the surface area of the wire. The latter can also be expressed via the diameter d and the length L of the alloy.
The second energy loss is the thermal conduction through the air. The corresponding rate of heat flow $\dot{Q}_A$ is given by

$$\dot{Q}_A = \frac{\kappa A}{l}\left(T - T_0\right) = \frac{\kappa\pi d_l L}{l}\left(T - T_0\right). \tag{7}$$

Here the temperatures are as defined above, κ is the thermal conductivity and A is the surface of the effective air layer, which is assumed to be a cylindrical surface and therefore can be expressed via its diameter d_l and again the length of the wire L. This cylindrical surface is given by the assumption of a limited laminar air layer, the effective air layer thickness. Inside this cylinder, the temperature is assumed to decrease linearly, and turbulent air on the outside leads to much faster heat transport away there. The distance between the surface of the wire with temperature T and the outer cylindrical surface of the effective air layer with temperature T_0 is expressed as the effective air layer thickness l (see Tab 1). The area used for the thermal conduction is not the same for the two sides of the effective air layer with different temperatures because of the cylindrical form. An approximation is to use half of the thickness of the laminar air layer added to the radius of the wire and use this as the diameter for the cylinder. Therefore d_l reads as follows

$$d_l = 2\left(r + \frac{l}{2}\right) = d + l. \tag{8}$$

Using the equations (5) - (7) the dependency between the current and the temperature can be calculated, namely

$$I^2 = \frac{\pi}{R_0 C_T}\left(\varepsilon\sigma d\left(T^4 - T_0^4\right) + \frac{\kappa d_l}{l}\left(T - T_0\right)\right). \tag{9}$$

In order to calculate the needed dependency for the KANTHAL D alloy the knowledge about the effective air layer thickness is required. The effective air layer thickness is determined by turbulence and thus mainly depends on the wire temperature independent of the used alloy. So values for it can be calculated with the rearranged Eq. (9)

$$l = \frac{\kappa\left(T - T_0\right)}{\frac{R_0 C_T I^2}{\pi d} - \varepsilon\sigma\left(T^4 - T_0^4\right) - \frac{\kappa}{d}\left(T - T_0\right)} \tag{10}$$

and the current-temperature-pairs for the NI80 alloy. The calculated values are listed in Tab. 1. The desired currents for the same temperatures for the KANTHAL D alloy can now be calcu-

Table 1: Dependency of the current on the temperature of the alloy NI80 from OMEGA for a diameter of 1 mm. The data is obtained from the data sheet OMEGA [2015]. The effective air layer thickness is calculated with Eq. (10).

Temperature [°C]	425	550	650	750	875	1100
Current [A]	8.32	10.17	12.48	15.11	18.06	24.03
Effective Air Layer Thickness [mm]	1.09	1.23	0.87	0.62	0.54	0.45

Table 2: Calculated dependency of the current on the temperature of the alloy KANTHAL D with a diameter of 1 mm from KANTHAL. The data is calculated as it is explained in the text and also taken from the data sheet KANTHAL [2016].

Temperature [°C]	425	550	650	750	875	1100
Effective Air Layer Thickness [mm]	1.09	1.23	0.87	0.62	0.54	0.45
Current [A]	7.24	8.72	10.59	12.74	15.08	19.82

lated using Eq. (9) and the determined values of the effective air layer thickness. They are listed in Tab. 2.

This data now only consists of six discrete points. In order to get an analytical expression for the current-temperature relationship a fit for the calculated data points in Tab. 2 is created using Eq. (9). The result is shown in Fig. 9. The errors were estimated by varying the emissivities of the alloys by 10 % each.

With these calculations the current is the only required observable to determine the temperature.

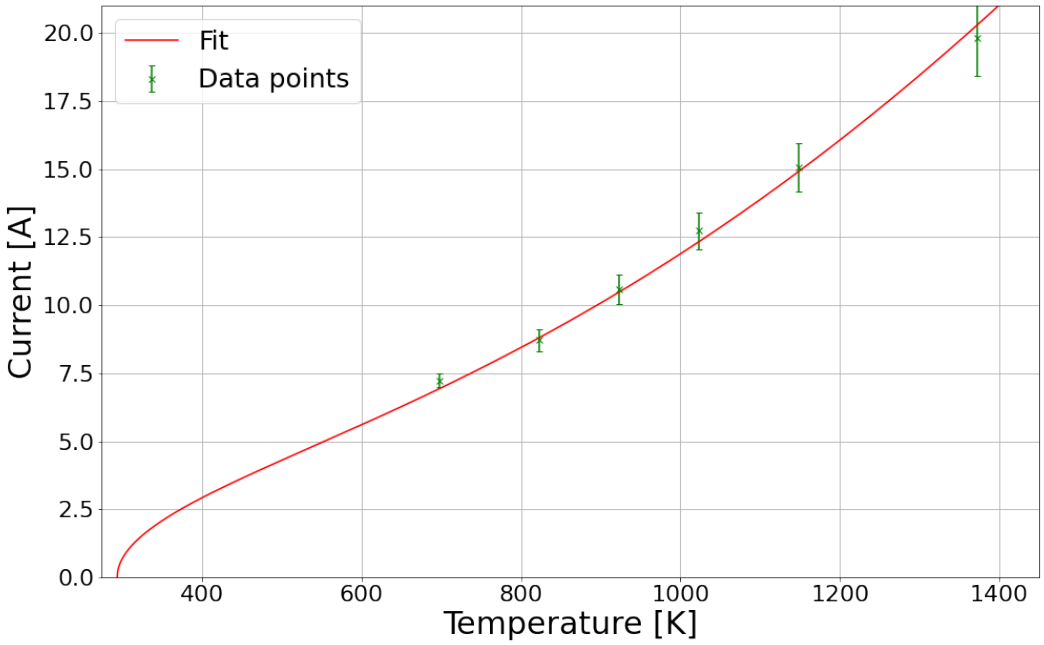

Figure 9: The current as a function of the temperature for the KANTHAL D alloy. The fit corresponds to Eq. (9) and the exact values of the data points can be seen in Tab. 2.

5.1.3 Setup

In order to carry out the calibration experiment the set up in Fig. 10 was used. It is a simple electrical circuit with the wire as the only remarkable resistance. The used power supply had a stable voltage of about 26.6 V. The voltage was additionally controlled with a multimeter throughout the experiment.

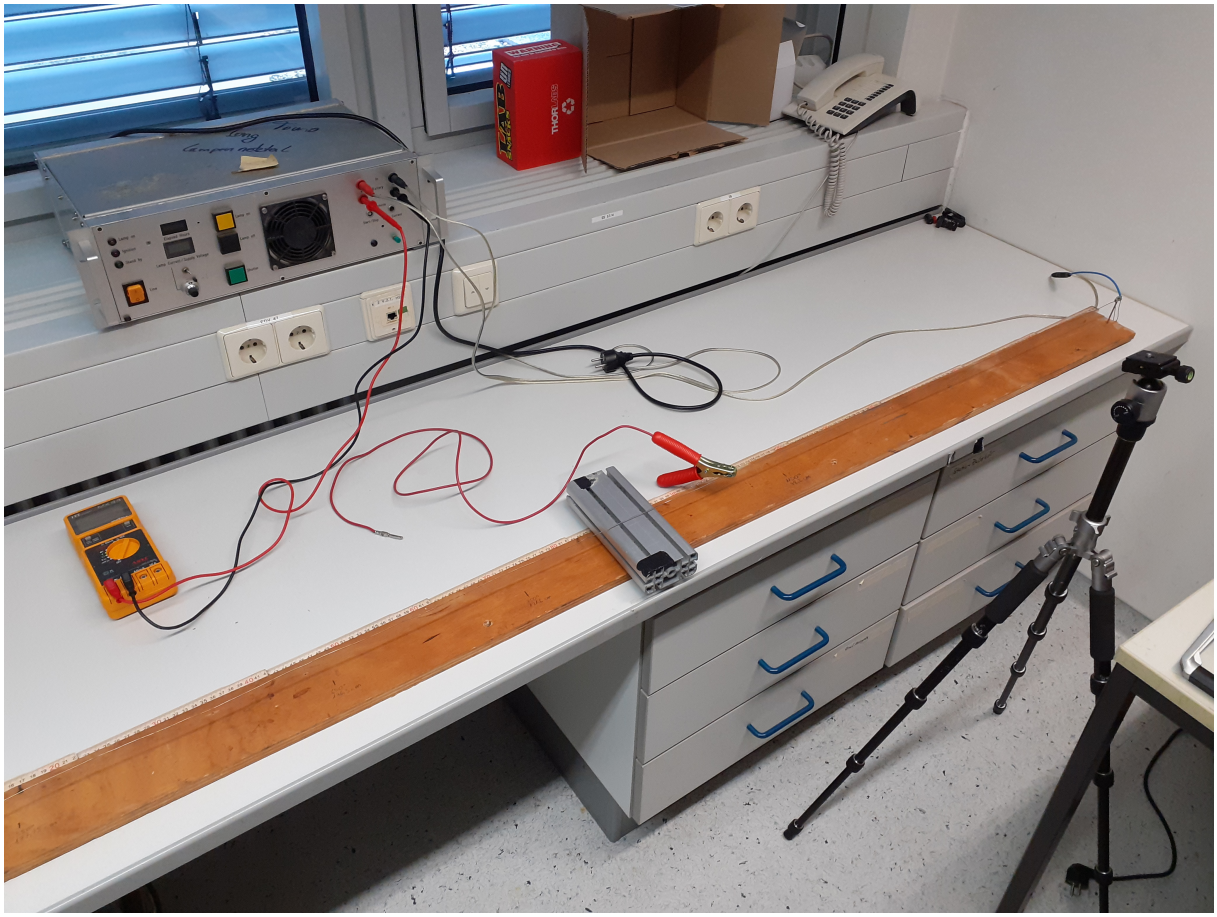

Figure 10: Set up of the calibration experiment.

To realise different temperatures it is necessary to vary the current. Because of the fixed voltage the effective length of the wire had to be changed. Therefore the wire was stretched over the length of a wooden plank without touching the surface of the plank in between its ends. One end of the wire was directly connected to the power supply. To close the circuit a clamp was connected to the wire as shown in Fig. 11. In this way, the length of the wire could be varied at will and so the current. The actual current was measured with a clamp-on ammeter, which measures the magnetic field induced by the current around the wire.
The camera was placed on a tripod and focused on one fixed spot of the wire. The focus was adjusted manually. The quality of the focus was found to affect the later evaluation noticeably. At the ends of the wire the temperature declines with the brightness (see e.g. Fig. 11). The area of decreasing temperature is very small and is not part of the observed, measured area, so that the thermal conduction through the direct contact of the wire with its suspension can be

neglected in the model above.
Using this set up several images were taken. The current and thereby the temperature was changed by rearranging the position of the clamp on the wire. For each temperature three images were taken, each with different shutter speed or F-number, to get more than one rb-ratio value per temperature with different settings. The shutter speed and the F-number do not change the rb-ratio itself.

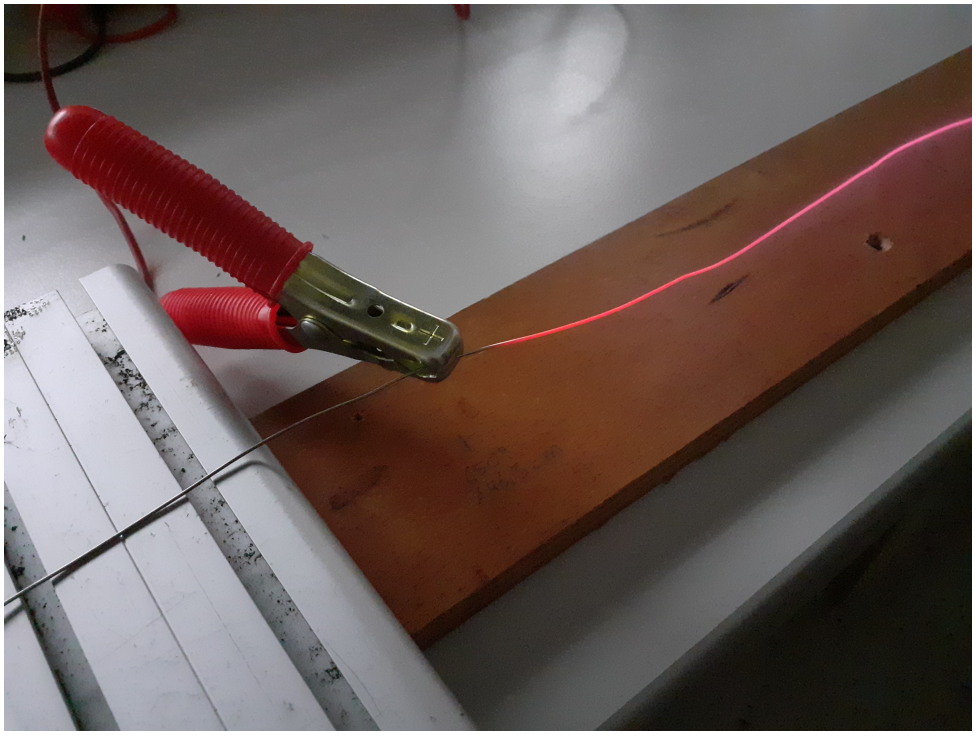

Figure 11: Picture of the connection of the wire and the clamp. The decline of the temperature towards the connection point can be nicely seen because of the lost in brightness. The change in color of the glowing wire is due to the aperture of the mobile phone camera, that was used, and has nothing to do with the actual temperature.

5.2 Data Analysis

Each image was analysed using Python3. If it is not mentioned separately every figure in this section is referred to the image for 15.45 A with a shutter speed of 1/800 s and a F-number of 7.1.
First the red and the blue pixel values are read out separately. The red values are generally higher than the blue values which reflects the supposed different transmissivity of the filters. An example for the red values can be seen in Fig. 12. It appears that the red values, for the blue values it is analogue, decrease the further they are at the edges of the image. This is the vignetting of the camera. This vignetting does not significantly effect the rb-ratio as it is corrected for in a later step (see section 5.2.1).
A zoom on the wire is provided by Fig. 13. Here it can be seen that the red values in the middle

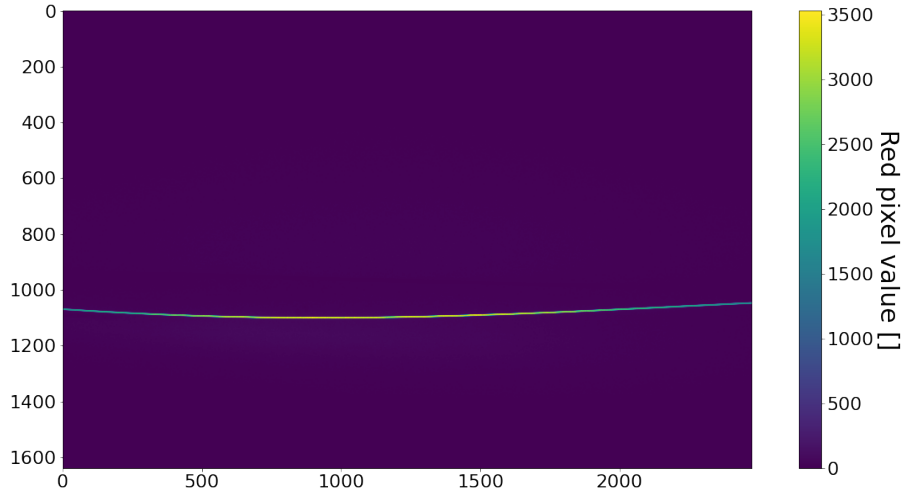

Figure 12: Red values of the image for 15.45 A with a shutter speed of 1/800 s and a F-number of 7.1.

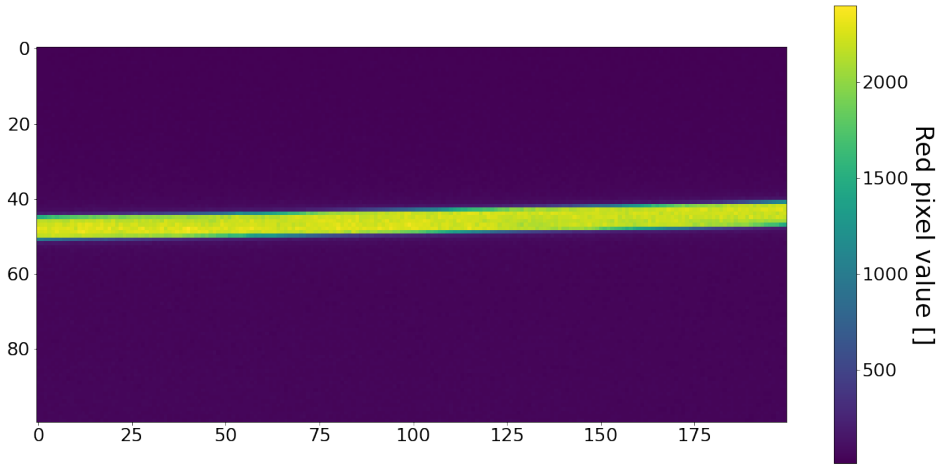

Figure 13: Zoom into the image shown in Fig. 12. The image was taken for 15.45 A with a shutter speed of 1/800 s and a F-number of 7.1.

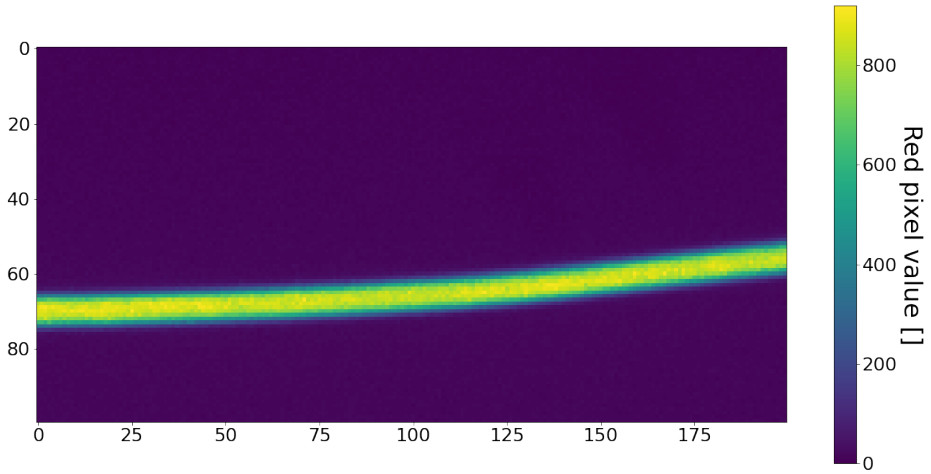

Figure 14: Part of red values of the image for 10.06 A with a shutter speed of 1/200 s and a F-number of 3.5 badly focussed.

of the wire are quite uniform while they differ at the wire edges. Especially when the position of the wire varies within the image and therefore an alteration in these rows is observable. This is explained by the color filter pattern of the pixels. The wire changes its position within the image continuously and so the single pixels are at some point only partly covered by the wire and hence the values are smaller. Because of the Bayer filter the red values are only taken every second row (also every second column) and so the spacial resolution is worse and the observed effect stronger, than it would be for the case where the red pixels would be next to each other.
As it was already mentioned the focus has to be adjusted accurately to get an acceptable result. An example for a bad focus is given in Fig. 14. The area of the edges, where the red values decrease, is spread much more broadly.
With the red and the blue values the rb-ratios can be calculated. An example of the results can be seen in Fig. 15. In the figure only a part of the whole image is shown (as e.g. in Fig. 13) in order to increase the visibility of the wire within the noise of the dark image parts. In Fig. 15 the wire can be nicely seen. The values in the middle of the wire are very uniform (also see Fig.16) and this is also the case towards the edges of the images. This indicates that the vignetting of the camera does not have a significant impact on the rb-ratios, which is desirable. To improve the measurement of the rb-ratios the effect of the vignetting will be corrected with the flat field correction in the next subsection.
In Fig. 16 a column of the image of the wire at 15.45 A with a shutter speed of 1/800 s and a F-number of 7.1 is depicted. The rb-ratio as well as the red value are shown for a part of the column where the wire is located. The red value directly indicates the location of the wire, because this value is almost zero for the cold surroundings but increases significantly at the wire, which has a much higher temperature. Also the red value is pretty constant for the wire,

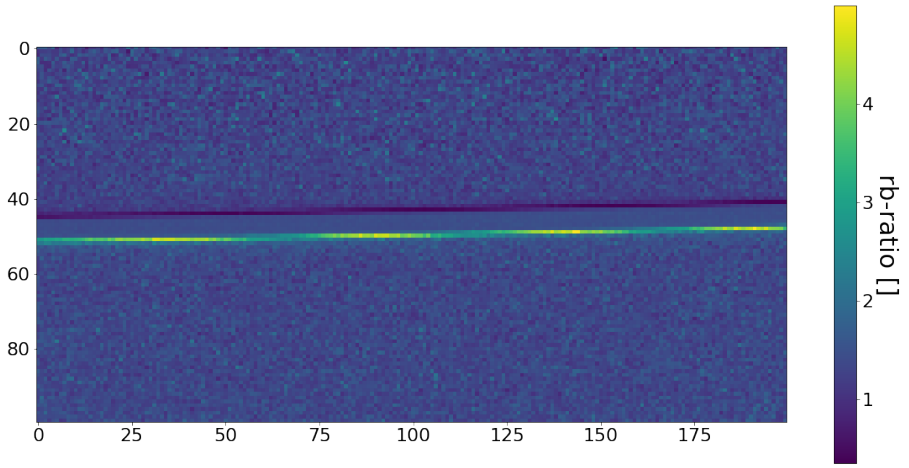

Figure 15: Part of rb-ratios of the image for 15.45 A with a shutter speed of 1/800 s and a F-number of 7.1.

as it should be because of the constant temperature of the wire. The rb-ratio therefore should be constant over the range of the wire because of the dependency on the temperature and this can be seen in Fig. 16. But this is only the case for the inner part of the wire and at the edges of the wire the rb-ratio deviates from the constant value. On the left edge in Fig. 16, which correspond to the upper edge of the wire in the image, the rb-ratio is lower and on the right edge (lower edge in the image) it is higher. This effect of the edges was already mentioned and explained before. So this figure shows some already known characteristics and also indicates again the dependency of the rb-ratio on the temperature.

In the case of a worse focus the wire would be blurred just as a consequence of the blurring of the red and blue values itself. Hence the values in the middle of the wire are less uniform and because of the higher background noise the wire itself is even harder do distinguish from the background. Also the effects on the edges, which will be discussed in the next paragraph, is blurred and it is much harder to separate this values from the desired ones.

At the edges of the wire the rb-ratios differ from the uniform values in the centre of the wire as well as from the background noise. They are higher at the lower edge and lower at the upper edge referring to the orientation of the image. This effect is again due to the Bayer filter pattern. The filter pattern of the used camera is a mosaic pattern rggb and so the related red and blue values, that are used to calculate the rb-ratios, are spatially shifted. For every red value the corresponding blue value is one row of pixels lower and one column of pixels further to the right. Therefore the blue values are always closer to the center of the wire when they are above it and further away when they are below it. Because of this orientation the rb-ratios differ at the edges. When the blue ratio is closer, the relative value is higher referring to the red value and hence the rb-ratio gets smaller. Conversely, the rb-ratio increases when the red value is closer to

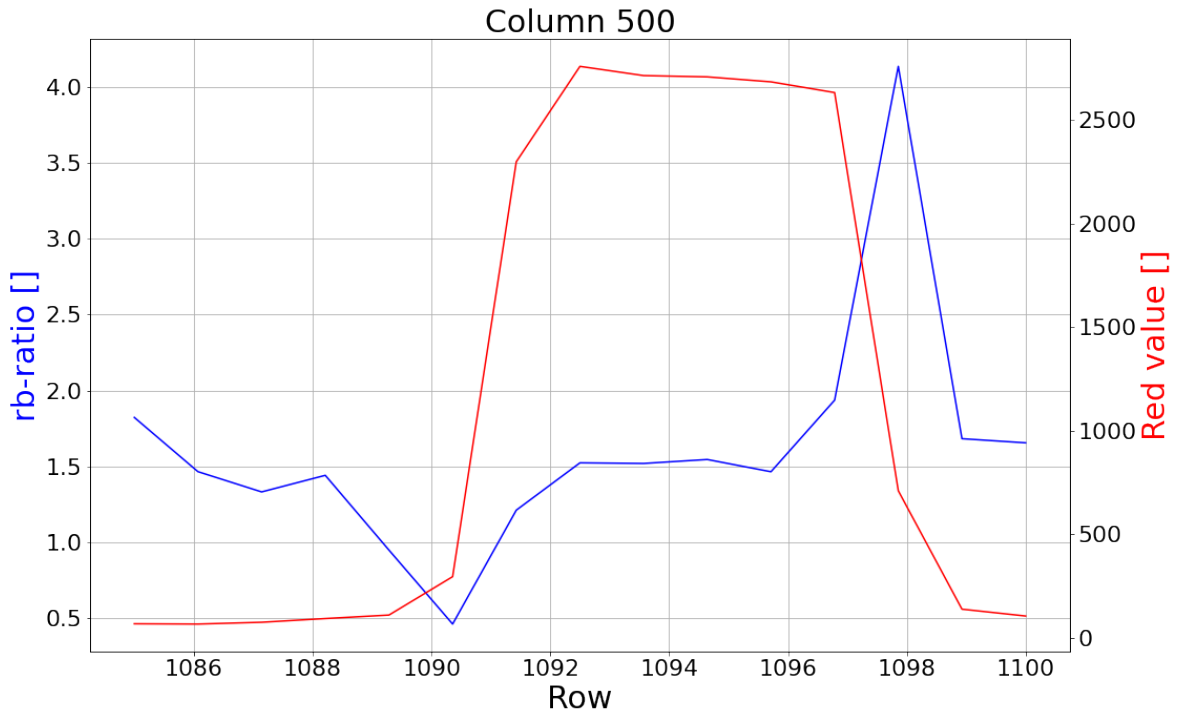

Figure 16: Cross section of rb-ratio and the red value of the wire at 15.45 A with a shutter speed of 1/800 s and a F-number of 7.1.

the center of the wire. This effect only appears at the edges of the wire where the red and blue pixels are not equally covered by the wire, in the centre of the wire this has no importance.
This explains the overall trend of the rb-ratios at the edges, but in Fig. 15 also a certain periodicity can be observed if the wire shifts in height. The reason for this is again the mosaic pattern. The general tendency of the lower rb-ratios at the upper edge and the higher rb-ratios at the lower edge was explained before. The periodicity has its origin in the spatial transition of the wire from one red-blue-pair to the next. As long as both the red and the corresponding blue pixel are at least partly covered by the wire the rb-ratio changes evenly from the constant rb-ratio to the maximum deviation when the wire is moving spatially. The maximum deviation in the rb-ratio is reached when one of the matching pixels is not covered any more but the other still is. Afterwards the rb-ratio changes evenly towards the background noise. Lets consider, for example, one row in the rb-ratio image at the lower edge of the wire while the wire is spatially moving up (see Fig. 17). Moving from the left to the right, starting with the constant rb-ratio of the middle of the wire, the blue pixels of this row are less and less covered by the wire and therefore the rb-ratio increases. This happens until the blue pixels are not covered any more, the maximum is reached. Afterwards the covering of the red pixels decreases until both the red and the blue pixels are not covered by the wire any more and hence the rb-ratios are now part of the background. On the upper edge of the wire this effect is analogue.
The rb-ratios are now plotted in a scatter plot against the corresponding red values like in Fig. 18. Here the previous discussed effects are clearly visible. The scatter plot is useful to choose the

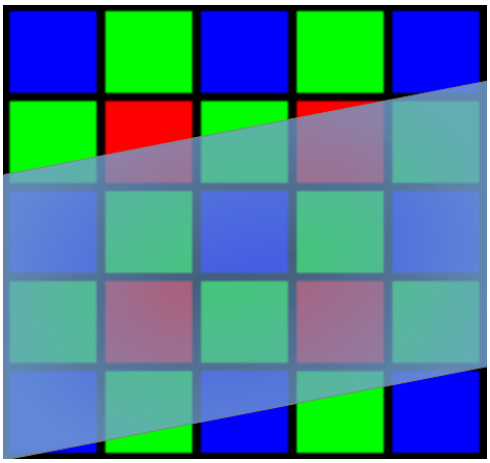

Figure 17: The Bayer filter pattern from Fig. 3 partly covered by the wire (depicted as transparent gray area). The wire and the size of the Bayer filter pattern are not to scale.

suitable rb-ratios, which are then used to relate to the corresponding temperature.
A better understanding of the overall appearance of the scatter plot and the different effects visible in this plot is necessary to choose the suitable rb-ratios.
Two arms leading to an accumulation of values with a certain rb-ratio at higher red values are observed in the scatter plot. These arms represent the effect of changing rb-ratio at the edges of the wire. The upper arm belongs to the values of the lower edge of the wire because the rb-ratios here are higher than in the centre of the wire and hence the lower arm belongs to the upper edge. Towards low red values, especially close to zero, the rb-ratios vary a lot. This is representing the background noise (i.e. the dark image part). Because of the low intensity small variations of the red or the blue value lead to large fluctuations in the resulting rb-ratio. The actual pixel values for the centre of the wire, which are of interest, can be found in the elongated part for higher red values where the two arms merge in a relatively constant rb-ratio (marked in Fig. 18). The stretching over a range of red values is caused by the vignetting. Hence the spots with lower red value belong to pixels that are closer to the edges of the image.
One can see that the rb-ratios of the elongated part are almost constant and therefore can be used to determine the rb-ratio for the corresponding temperature (we assume a constant wire temperature across the image). As it is already mentioned before this will be improved by the flat field correction. The appearance of the scatter plot has in general the same shape for different temperatures and also for different shutter speeds and F-numbers at the same temperature. Fig. 19 shows a scatter plot for the same current but a different shutter speed as it was used in Fig. 18. The range of the red values changes with the shutter speed but the rb-ratios for the middle of the wire stay the same (marked in Fig. 19). This is what one would expect. Because of the different shutter speed the intensity changes, this can be recognized by the red values, but the rb-ratios do not change because the change in intensity affects the red values as well as the blue values and does not make a difference for the ratio. The same holds for changing the F-number. If the focus of the image is bad the two arms are not so well pronounced and so the

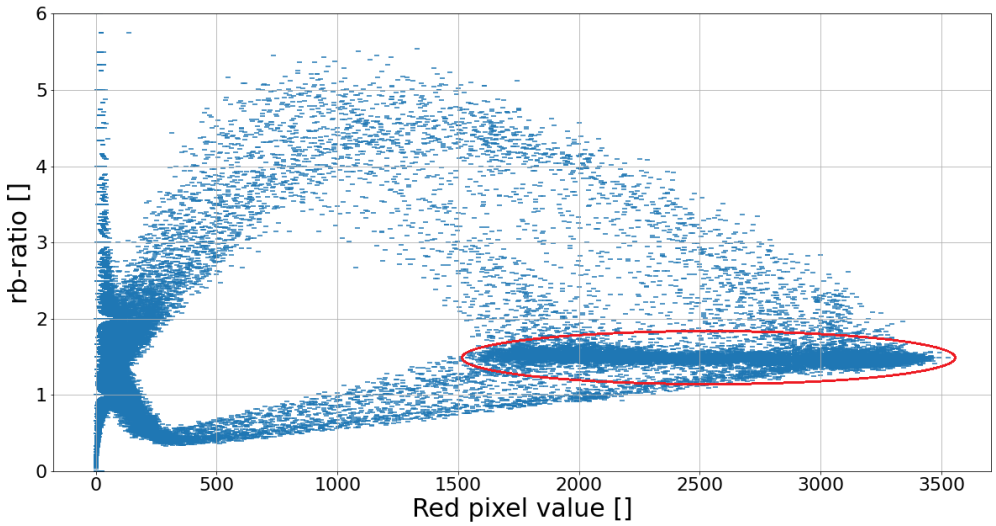

Figure 18: Scatter plot of the rb-ratios and the corresponding red values of the image for 15.45 A with a shutter speed of 1/800 s and a F-number of 7.1. The rb-ratios related to the centre of the wire are marked.

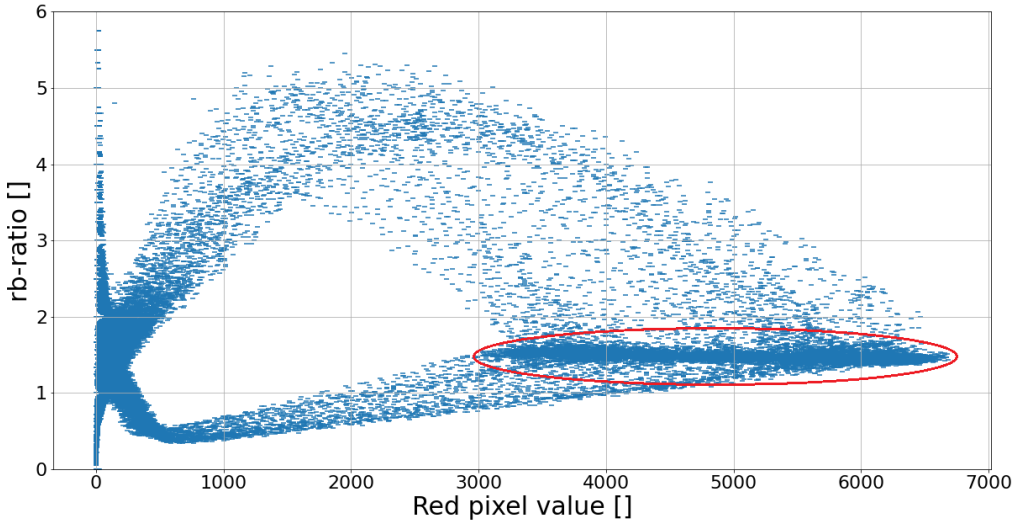

Figure 19: Scatter plot of the rb-ratios and the corresponding red values of the image for 15.45 A with a shutter speed of 1/400 s and a F-number of 7.1. The rb-ratios related to the centre of the wire are marked.

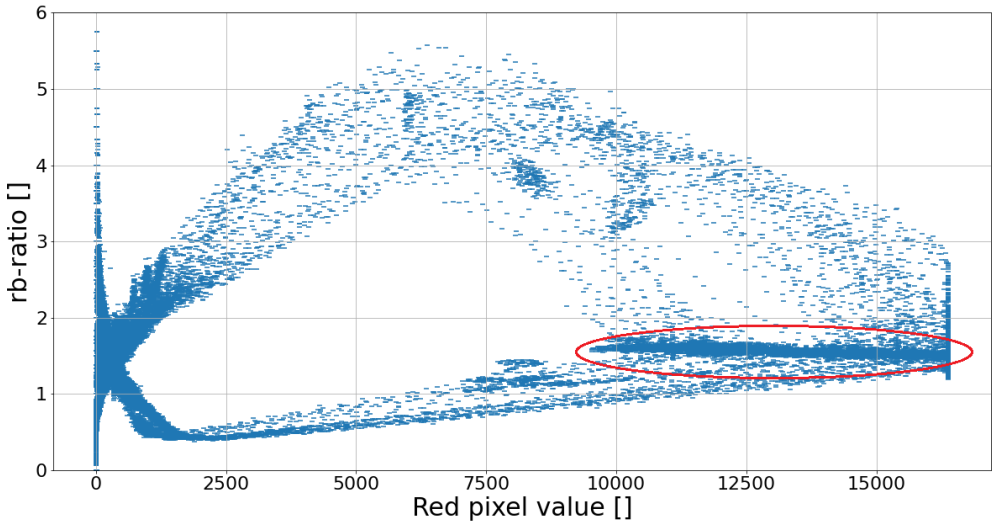

Figure 20: Scatter plot of the rb-ratios and the corresponding red values of the image for 17.7 A with a shutter speed of 1/400 s and a F-number of 7.1. Some of the red pixels are saturated. The usable rb-ratios related to the centre of the wire (marked) are limited by the maximum red value.

rb-ratios from interest are a lot harder to define.

An example for a scatter plot where the saturation is reached is given in Fig. 20. The general structure of the scatter plot is the same as before but the values are cut off at a maximum value of 16383, which is the maximum value for any pixel for the used camera. Because of the filter characteristics of the red and the blue pixels the red pixels are first saturated while the blue ones are not. Fig. 21 shows the same rb-ratios with the corresponding blue values. Is shows nicely that the blue values are not saturated, but the maximum of the rb-ratios is smaller the higher the blue ratios get, because of the reached maximum red value. For higher blue values it is harder to determine the still unsaturated rb-ratios, so the scatter plot with the red values is more useful, because of the direct cut at the maximum value. This also indicates that the red values are saturated while the general structure again is the same as before. The rb-ratios for pixels with saturated red values are lower respective to the not saturated pixels. The rb-ratio for the other none saturated pixels could still be used for temperature determinations. The calculation of the rb-ratio just using the unsaturated values still yields a good rb-ratio close to the ratio of the total unsaturated images.

The rb-ratios of interest are located at the elongated part where the two arms merge in the scatter plot. These values have to be selected to get an average of the rb-ratio which then serves as the rb-ratio for the corresponding temperature. To achieve this first a threshold for the red values was chosen to cut off the background noise and the lower parts of the to arms. Then, to separate the desired values from the rest of the arms, a Gaussian fit for the rb-values was used and every value outside the 2σ-area was sorted out. With this final ensemble of rb-ratios the average value

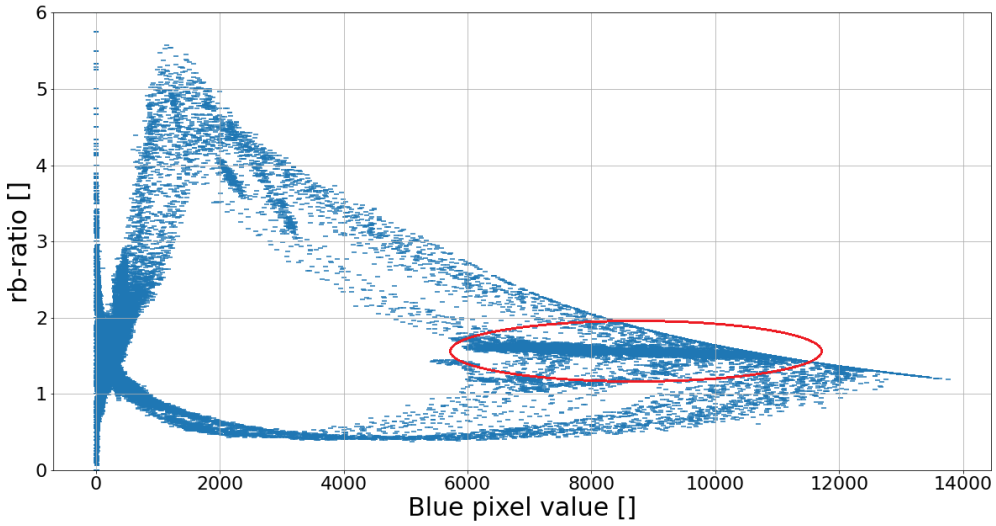

Figure 21: Scatter plot of the rb-ratios and the corresponding blue values of the image for 17.7 A with a shutter speed of 1/400 s and a F-number of 7.1. Some of the red pixels are saturated. The usable rb-ratios related to the centre of the wire (marked) are limited by the maximum red value.

was determined. In Fig. 22 the with the red value threshold and the 2σ-area of the Gaussian fit selected rb-ratios are depict, whereas the discarded ratios are set to zero. It shows that the ratios over the whole length of the wire and hence all relevant pixels are used.

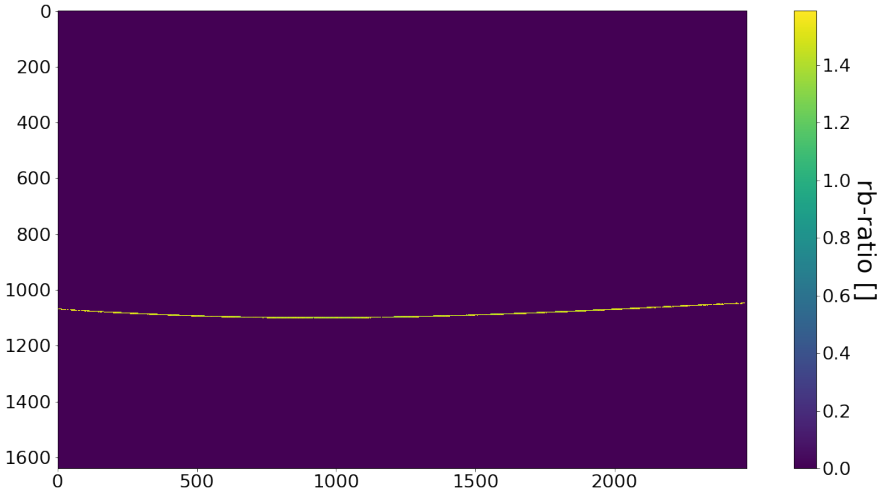

Figure 22: Selected rb-ratios of the image for 15.45 A with a shutter speed of 1/800 s and a F-number of 7.1. The selection was done as it is described in the text.

This evaluation was done for every image to get three averaged rb-ratios for every measured temperature. The three values are always nearly the same and the results can be seen in sec-

tion 5.3. The threshold for the red values to select the range of values of interest has to be selected individually for each image according to its saturation, which is variable because of the use of different shutter speeds and F-numbers.

5.2.1 Flat Field Correction

As it was mentioned before the rb-ratios of the wire are almost constant, but in fact they vary slightly over the range of the red values. To compensate this effect a flat field correction (FFC) was done. This process corrects for e.g. the vignetting, which was mentioned above.
In order to do this correction a set of equally illuminated images for every F-number is required. To achieve this an integrating sphere was used. In this sphere the light of a light source gets diffuse and hence an image of the inner of the sphere yields an equally illuminated image, a flat field image. This can the be used to correct for the vignetting using the equation (4).

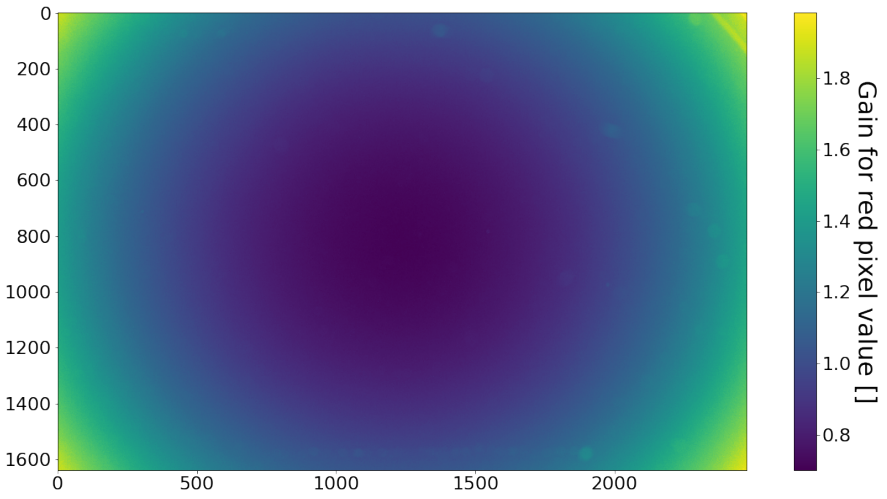

Figure 23: Correction image of the red pixel values for the F-number 7.1.

For the in this thesis used camera the dark fields are fluctuations of the values around the zero to small positive values, because there are no negative values recorded by the sensors. Because the efficiency of the sensors is not perfect and hence not equal to one, the noise should equally fluctuate around a certain value. This is not the case for the darks fields, because negative values are not recorded and for this camera no offset is used. The averaged noise would be a small value. So the correction with the dark fields would yield a shift of the values of the raw and the flat field images, but the values of the dark fields are negligibly small. Hence is not used in this correction. Thus the formula (4) is used without the dark field D (equal to setting D to zero).
For every F-number ten images were summed up to reduce the photon shot noise. With the summed up images the correction images for the corresponding F-numbers where calculated, so that the raw images just have to be multiplied with these correction images. This was done

separately for the red and the blue pixels. An example of the correction image of red pixels for the F-number 7.1 is given in Fig. 23.

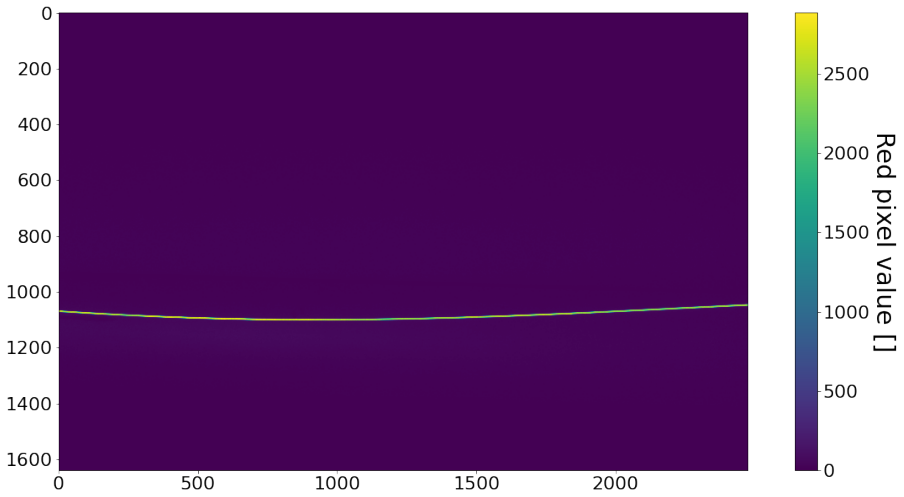

Figure 24: Red values of the image for 15.45 A with a shutter speed of 1/800 s and a F-number of 7.1 after the flat field correction.

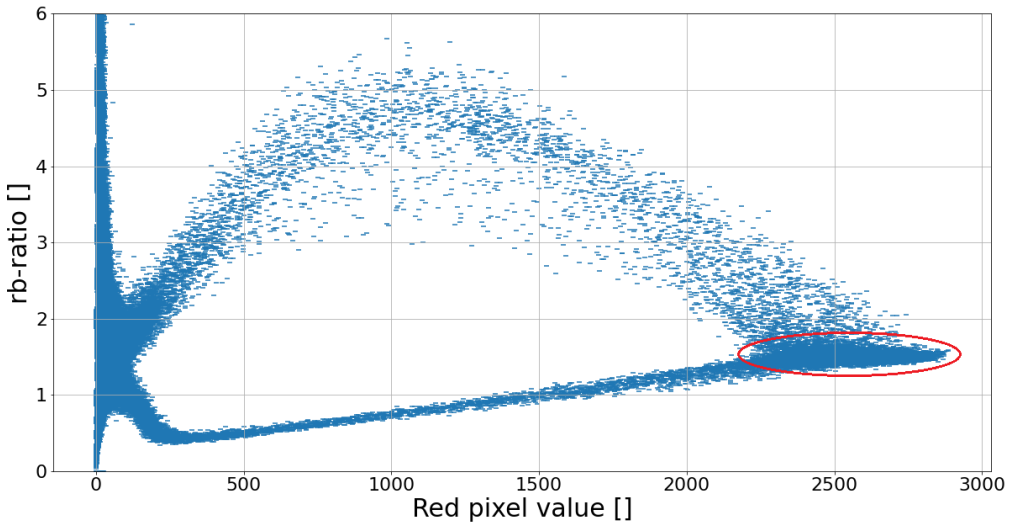

Figure 25: Scatter plot of the rb-ratios and the corresponding red values of the image for 15.45 A with a shutter speed of 1/800 s and a F-number of 7.1 after the flat field correction. The rb-ratios related to the centre of the wire are marked.

With the corrected images the same evaluation as above was done. The effect of the vignetting is gone. This can be seen in Fig. 24. The red values are constant over the whole length of the wire in contrast to the not corrected image in Fig. 12. The effects at the edges of the wire are still visible and still have to be taken into account. Hence the arms in the scatter plot in Fig. 25 are

still there and the general appearance is the same. In contrast to before (Fig. 18) the spreading over the red values is much smaller. As mentioned before the elongated part was caused by the vignetting, which the image is now corrected for. That is why the rb-ratios of the wire are now in a compact group (see marked rb-ratios in Fig. 25) and also the slight shift of this rb-ratios, which was the reason to do this correction, is gone. The expanse of the arms in the scatter plot is also a lot smaller, because this was also caused by the vignetting.
The further selection and calculation of the relevant rb-ratios for every image was done as before. The ratios determined with the FFC are the values that were used as results. In the following the rb-ratios are always the ones with the FFC unless it is explicitly stated.

5.3 Results

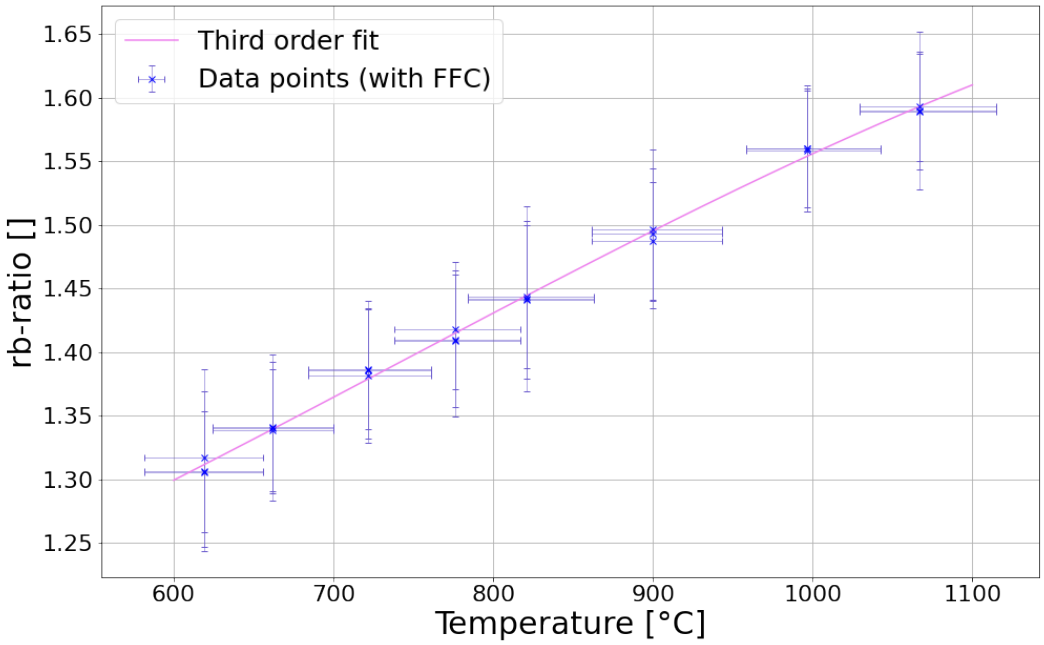

Figure 26: Data points of the rb-ratios for the corresponding temperatures with fit. The temperatures were calculated from the measured current as it is explained in section 5.1.2.

The rb-ratios calculated as explained before together with the temperature determination as in section 5.1.2 yield a calibration curve to transform the measured rb-ratio to a corresponding temperature. The received data points with the accompanying errors can be seen in Fig. 26. The errors for the rb-ratios are the received σ-values of the used Gauss fits. For the errors of the temperature the fit of the dependency of the current on the temperature in section 5.1.2 was varied. The emissivities of the alloys, used to calculate the data points for the fit, were varied by ± 10 %. Doing so the maximum and minimum deviation of the fit were calculated and then used to determine the maximum and minimum temperatures for the same current referring to

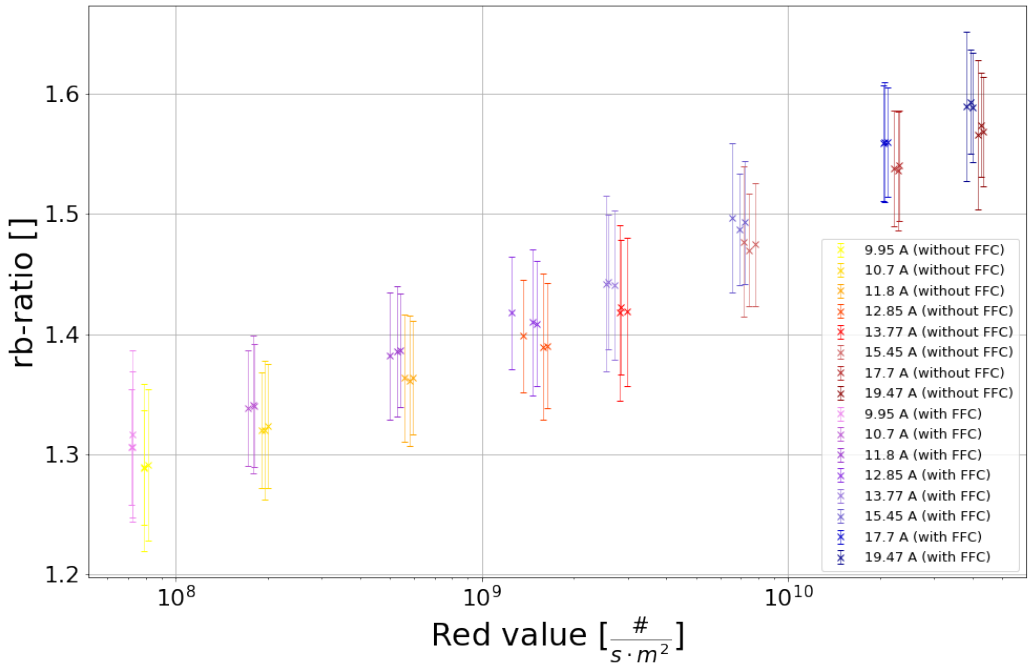

Figure 27: The rb-ratio plotted over the red value normalized per second and square meter.

this variation.

The data points were then used to create a fit. Because the exact filter curves of the sensors are unknown and hence the form of the fit is also not known, a polynomial fit of the third order was used. This fit describes the dependency of the rb-ratios on the temperature quite well, even if one would have smaller errors. The general position of the data points, not considering the errorbars, indicate the possibility to measure the temperature with the rb-ratios. Also the data points reflect the dependency of the rb-ratio on the temperature of the simplified model done before in section 3. Therefore the behaviour of the calibration is the desired one.

The dependency of the rb-ratio on the temperature can also be seen via the dependency of the rb-ratio on the red values (or alternative the blue values). The intensity of the light emitted by an object is larger for a higher temperature. The intensity is directly proportional to the red value (and the blue value) detected by the sensors of the camera. Hence a higher temperature leads to a higher red (or blue) value which also should correlate to a certain rb-ratio as we have seen before (see e.g. Fig. 16).

The general dependency of the rb-ratio on the red value can also be seen in Fig. 27. This figure shows the rb-ratio with the corresponding red value, while the latter was normalized for the exposure time and the aperture size, because besides the temperature itself the time and the area of incoming light also impact the intensity and therefore the red value. Hence, to make all different shutter speeds and F-numbers comparable, the normalization is needed. The red value depicted is always the average red value of the same group of pixels that were used to calculate the rb-ratio. The several groups of three points each belong to one temperature (for

every temperature three images were taken). Because of the same temperature for each group the rb-ratios should be closely together like in Fig. 26. The same holds for the red values, because of the normalization of the time and area they are only affected by the temperature as well. The form of the positions of the data points in Fig. 27 matches the expected form that already appeared at the simplified model in section 3, even if the red values differ because of the normalization and the different approach to calculate them in the model and here. Hence this is also consistent with the dependency of the rb-ratio on the temperature.
In Fig. 27 there are the data points with the FFC and also without the FFC depicted. This is done to see in which way the FFC does change the characteristics of the dependency. In general there is a shift between the two methods in both the rb-ratio and the red value. The representation in Fig. 27 is chosen, because both effects can be seen here while the representation in Fig. 26 only would show the shift in the rb-ratio. The shift in the red value in Fig. 27 is due to the correction factor used in the FFC (see Fig. 23). The wire in the calibration images is always located close two the middle of the height of the image and goes from the left to the right edge of the image. Therefore one could guess that the value of the correction image for the most pixels of the wire, which are used to get the rb-ratio and also the average red value, is smaller than one. This is in fact the case and so the red value of every image is slightly lower with FFC than without, as it can be seen in Fig. 27. Also the rb-ratio of the images with FFC is always slightly higher. This effect is produced by the different strength of the FFC for the red and the blue pixels. The correction images are not the same for the different filters, because they differ in their transmitting wavelength. So there is also a shift in the blue value that is different to the one for the red value and hence the final rb-ratio is changed as it can be seen. Because this effect is originated in the correction images and they will be applied for every further image that will be evaluated the rb-ratio shift between with and without FFC does not change the final result of the temperature for the same image.
Overall the determination of the temperature by calculating the rb-ratio of the images is possible and yields the spatial distribution of the temperature for temperatures in the range of 600 to 1100 °C with an uncertainty of 130 °C, which is based on cautious assumptions for the error.

5.3.1 Example: Image of a Lava Lake at the Nyiragongo

As an exemplary application of this method a image of a lava lake from Nyiragongo volcano, Democratic Republic of Congo, was analysed. The image was taken by Jonas Kuhn on the 12.02.2020 at Nyiragongo. The raw image was read out the in same way as the images used for the calibration and with the received red and blue values the rb-ratio was calculated analogue. Then the calibration curve from Fig. 26 was used to determine the corresponding temperatures. The original visualized image and the result of the temperature distribution can be seen in Fig. 28. The temperature was only determined for rb-ratios with certain red values, that where larger then the chosen threshold, to prevent a big influence of the scattered light in the smoke. In principle, other light sources (e.g. sunlight) could also be excluded based on their different

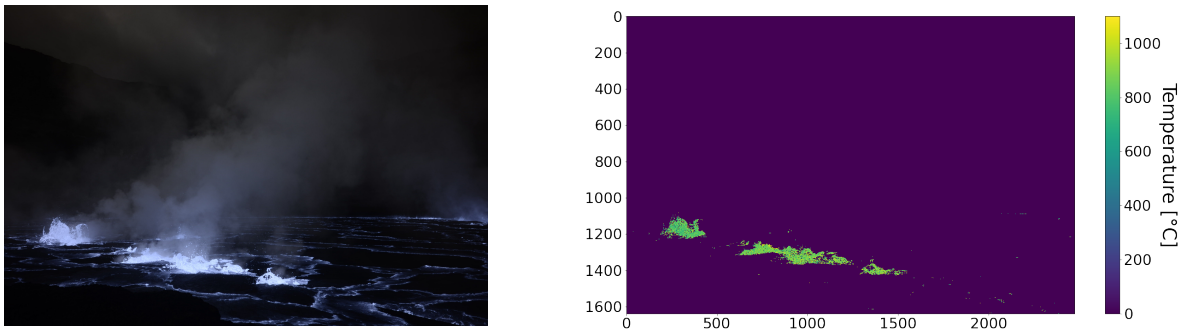

(a) (b)

Figure 28: (a) Image of a lava lake at the Nyiragongo taken by Jonas Kuhn on the 12.02.2020 and (b) the corresponding spatial temperature distribution. Only mainly undisturbed areas, which were also hot enough, where taken into account. The other pixels where set to 0 °C.

rb-ratio. This is why only the active areas of the lava lake have an assigned temperature and the other areas are treated as 0 °C, even though this is not the actual temperature. The assigned temperatures have an error of about 120 to 130 °C and the mean temperature of the in Fig. 28 (b) shown parts of the lava is 850 °C.

It can be seen that the determination of the temperature with this camera calibration can be done with high spatial resolution. The precision of the temperatures and the more precise selection of the rb-ratios, and so the temperatures, that can be determined accurately, can be further improved by using better selection methods and models to reduce negative influences. A suggestion for improvement would be the calibration with the respective magma. This will be further discussed in the next section.

6 Discussion and Outlook

In this thesis a digital camera was calibrated in order to use it as a thermal camera for high temperatures of about 600 to 1100 °C. The calibration showed that a determination of the temperature is feasible by using the rb-ratio of the raw images taken with the camera. The error, based on cautious assumptions, amounts to about 130 °C.
A direct dependency of the rb-ratio on the temperature was established (Fig. 26). Also the dependency of the rb-ratio on the red value (Fig. 27) reflects this. Both of these results agree with the expectations from the simple model described in section 3). Also high and constant red values, which indicate a hot object, go along with a constant rb-ratio (Fig. 16).
An effect that appeared in the calibration was that the rb-ratio rapidly changed at the edges of the wire. Hence, the edges of objects generally require cautious treatment and might be excluded from measurements. For different objects similar effects can occur, because of the characteristic Bayer filter pattern. These kind of effects also not only depend on the form of the investigated objects, but also depend on the Bayer pattern of the used camera sensor itself. This has to be considered, when the rb-ratios are selected. The noise can be reduced by using a threshold for the red or the blue value, so the cold temperatures are sorted out. But because of such effects an optimal selection method has to be found for every case separately. Also the calibration has to be done for every camera individually, because of the different color filter curves. They can differ for every manufacturer and camera model. This can change the final calibration curve (Fig. 26) and can also influence the range of the rb-ratio over the same temperature range. Also it has to be mentioned that a camera with accessible raw images is needed. The data types of raw images can also differ for different manufacturers.
The flat field correction, that was applied, corrects for any influences of the optical system and pixel-to-pixel sensitivity variations. This correction is recommendable, because dust or scratches could lead to undesirable errors. If the response of sensor of the camera (the digital number) has an offset, the dark field also could be used, but this is not necessary because the values are negligibly small. An integrating sphere, as it was used, is a good way to perform the flat field correction, because it is reliable and a rather easy way to get flat field images.
The accuracy of the rb-ratio could also be improved by binning of the pixels. Four pixels for example could be added together to improve the signal-to-noise-ratio. To further improve this method a knowledge of the exact filter curves would be beneficial. If they are known the optimal wavelength range used in the NIR could be determined, to get the optimal dynamic range of the rb-ratio for the same temperature range.
On the other hand, the calibration method could be improved or a different method could be used. In this thesis a heating wire was used and the temperature was determined by the applied current. The current-temperature relationship was determined by a simple model (see section 5.1.2). Because the heat transfer of this model was approximated, the determination of the temperature could be improved by modelling this heat transfer from the wire in more detail. A good

alternative to this calibration method would be the calibration with a already calibrated black body furnace like it was done by Wilkes et al. [2018]. This also would improve the accuracy of the temperature for the calibration compared to the heating wire. There might also be the possibility to calibrate the camera by controlled heating of rock with the composition of the to be measured magma [see Li et al., 2021].
The investigation of the image from a lava lake at the Nyiragongo with the calibrated camera shows the possibilities of this method. This low-cost technique offers the possibility to get a high spatial resolution of the temperature distribution by 'point and shoot' and offers a method to investigate high dynamic situations. Because of the wide range of shutter speeds and F-numbers (aperture sizes), the saturation of the sensors can be controlled by the user and this enables to use the optimal saturation range for a wide temperature range.
This method stands not only in contrast to the more expensive available thermal cameras, but also to other approaches using the NIR like in Wilkes et al. [2018], because the optical system does not have to be changed, except for the 'hot mirror', and it is a still a compact and robust camera. Still there are some problems, that also appear for other systems, when this is used in field measurements, in particular the absorption in the viewing path and scattering of light, especially from the sun. To correct for this effects, models can be used like in Wilkes et al. [2018]. Additionally the emissivity of the lava plays a crucial role to determine the temperature of the lava. One has to take into account that the emissivity also varies for different temperatures as it was investigated by Li et al. [2021].
Overall a commercial digital camera, which is sensitive in the NIR, can be used as a thermal camera for high temperatures just by replacing the 'hot mirror' with a NIR pass filter and a calibration. So this method is a promising alternative to the rather expensive systems operating in the mid- and long-infrared and also to other low cost NIR systems. With further improvements this method also has a large potential as a low cost thermal camera.

Appendix

Here the data acquisition from the camera will be described. As it was mentioned a camera with accessible raw images is needed. To acquire this raw images and to transform it into a usable format the Python3 package *rawpy* was used [Riechert, 2014]. It enables to read kinds of raw image data types, including .NEF.

```
#Import rawpy
import rawpy as rp

#Read raw image
raw=rp.imread('filename.NEF')

#Useful and needed information
print('Value of the first pixel:',raw.raw_value(0,0))       #Raw pixel value of the selected pixel
print('Color of the first pixel:',raw.raw_color(0,0))       #Color index of the selected pixel
print('Color description:'       ,raw.color_desc)           #Color description
print('Number of colors:'        ,raw.num_colors)           #Number of colors
print('Color pattern:'           ,raw.raw_pattern.tolist()) #Bayer pattern with numbers
print('White level:'             ,raw.white_level)          #Maximum pixel value
print('Height:'                  ,len(raw.raw_image))       #Height of the raw image
print('Width:'                   ,len(raw.raw_image[0]))    #Width of the raw image
```

Figure 29: Exemplary representation of the most important commands working with *rawpy* [Riechert, 2014] in the frame of this thesis. The detailed descriptions of the single commands are in the text below.

In Fig. 29 the most important commands from *rawpy*, that were needed in this thesis, are shown as an example. After the import in the command *imread* can be used to open the file and makes it accessible for further processing. The data of the single pixels can be acquired by the commands *raw_value* and *raw_color*. The output of the first one if the raw pixel value, which is a digital number referring to the sensor responds of the selected pixel to the incident light. The latter command returns the color index (0, 1, 2 or 3) of the selected pixel. The color associated with the index can be acquired with *color_desc*. The output for the in this thesis used camera was 'RGBG', which means that 0 is red, 1 is green, 2 is blue and 3 is again green. The two 'G' do not necessarily mean, that it is the same green. Cameras can have two different greens. The number of colors is returned by *num_colors*. For the used camera it was 3, so that the greens in this case are the same. The colors are correlated to the Bayer pattern of the camera sensors and it can be acquired by *raw_pattern.tolist*(). Here it was the first 2x2 pixel group with red pixel in the top left corner and the blue one in the bottom right corner. In general the information of the green pixels are not from interest for the used method, but the knowledge of the position of the red and blue pixels is needed to perform the calculations. The command *white_level* returns the maximum pixel value. If this value is reached the pixel is saturated. The range of the pixel values for the used camera was from 0 to 16383. At last the command *raw_image* returns an 2D ndarray, which was only used to determine the dimensions of the raw image. It has to be taken into account, that this array still have a margin with further information of the raw image. With the information acquired with the above explained commands, the single red and blue

pixels where identified, the raw values were read out and the rb-ratio was calculated for every red-blue-pixel pair. The rb-ratio were stored again in a 2D array with half the dimensions of the original image, because of the arrangement of the red and blue pixels.

Acknowledgements

I would like to express my thanks to Professor Ulrich Platt for the opportunity to write my bachelor thesis in his group. His extensive knowledge was very helpful throughout this thesis.
I would also like to thank Professor Werner Aeschbach for being my second examiner.
I also thank Nicole Bobrowski for many helpful comments and questions, that led to a better understanding in many cases. A big thanks also to Christopher Fuchs for the support building up the calibration experiment and contributing with many ideas to improve this work.
I owe the greatest thanks to Jonas Kuhn, who mentored me during the whole time of this thesis. The help with every question that emerged and him sharing his knowledge of the topics of this work were crucial.
Finally, I would like to thank Alexander “Minky” Bryant for proofreading.

References

B. E. Bayer. Color image array. *U.S. Patent 3 971 065*, July 1976.

W. Demtröder. *Experimentalphysik 1*. Springer Berlin Heidelberg, 2015. doi: 10.1007/978-3-662-46415-1.

W. Demtröder. *Experimentalphysik 3*. Springer Berlin Heidelberg, 2016. doi: 10.1007/978-3-662-49094-5.

A. Ducharme, A. Daniels, E. Grann, and G. Boreman. Design of an integrating sphere as a uniform illumination source. *IEEE Transactions on Education*, 40(2):131–134, may 1997. doi: 10.1109/13.572326.

L. P. Flynn, P. J. Mouginis-Mark, J. C. Gradie, and P. G. Lucey. Radiative temperature measurements at kupaianaha lava lake, kilauea volcano, hawaii. *Journal of Geophysical Research: Solid Earth*, 98(B4):6461–6476, apr 1993. doi: 10.1029/92jb02698.

E. R. Fossum and D. B. Hondongwa. A review of the pinned photodiode for CCD and CMOS image sensors. *IEEE Journal of the Electron Devices Society*, 2(3):33–43, may 2014. doi: 10.1109/jeds.2014.2306412.

T. M. Gerlach. Volcanic sources of tropospheric ozone-depleting trace gases. *Geochemistry, Geophysics, Geosystems*, 5(9), 2004. doi: 10.1029/2004gc000747.

KANTHAL. Kanthal D, Oct. 2016. URL `https://www.tme.eu/Document/d7ff1ae3db5e4119c82ac25e72be697d/kanthal-d.pdf`.

H. Li, J. Andujar, A. Slodczyk, D. D. S. Meneses, B. Scaillet, P. Echegut, J. Biren, and C. Oppenheimer. Spectral emissivity of phonolite lava at high temperature. *IEEE Transactions on Geoscience and Remote Sensing*, pages 1–15, 2021. doi: 10.1109/tgrs.2021.3104657.

K. Mangold, J. A. Shaw, and M. Vollmer. The physics of near-infrared photography. *European Journal of Physics*, 34(6):S51–S71, oct 2013. doi: 10.1088/0143-0807/34/6/s51.

J. Maschal, Y. R. A., R. S. S., K. Joe, F. Keith, C. Jonathan, and Ted. Review of bayer pattern color filter array (CFA) demosaicing with new quality assessment algorithms. Technical report, jan 2010.

V. V. Nieuwenhove, J. D. Beenhouwer, F. D. Carlo, L. Mancini, F. Marone, and J. Sijbers. Dynamic intensity normalization using eigen flat fields in x-ray imaging. *Optics Express*, 23 (21):27975, oct 2015. doi: 10.1364/oe.23.027975.

Nikon. *Nikon DIGITAL CAMERA COOLPIX A Reference Manual*. Nikon Corporation, 2013.

OMEGA. Ni80 Heizwiderstandsdraht aus Nickel-Chromlegierung, Feb. 2015. URL `https://www.omega.de/Temperature/pdf/ni80.pdf`.

C. Oppenheimer, B. Scaillet, A. Woods, A. J. Sutton, T. Elias, and Y. Moussallam. Influence of eruptive style on volcanic gas emission chemistry and temperature. *Nature Geoscience*, 11 (9):678–681, aug 2018. doi: 10.1038/s41561-018-0194-5.

M. Riechert. rawpy, 2014. URL `https://github.com/letmaik/rawpy`.

T. Roberts, G. Dayma, and C. Oppenheimer. Reaction rates control high-temperature chemistry of volcanic gases in air. *Frontiers in Earth Science*, 7, 2019. doi: 10.3389/feart.2019.00154.

J. Stefan. Über die Beziehung zwischen der Wärmestrahlung und der Temperatur. *Sitzungsber.Kaiserl.Akad.Wiss.Math.Naturwiss.Cl.II.Abth. 79 (1879) 3, 391-428*, 1879.

T. Wilkes, L. Stanger, J. Willmott, T. Pering, A. McGonigle, and R. England. The development of a low-cost, near infrared, high-temperature thermal imaging system and its application to the retrieval of accurate lava lake temperatures at masaya volcano, nicaragua. *Remote Sensing*, 10(3):450, mar 2018. doi: 10.3390/rs10030450.

Erklärung

Ich versichere, dass ich diese Arbeit selbstständig verfasst und keine anderen als die angegebenen Quellen und Hilfsmittel benutzt habe.

Heidelberg, den 23.01.2022, Joshua Mutz